

Dislocation Avalanches: Earthquakes on the Micron Scale

Péter Dusán Ispánovity^{a,*}, Dávid Ugi^a, Gábor Péterffy^a, Michal Knapek^b,
Szilvia Kalácska^a, Dániel Tüzes^a, Zoltán Dankházi^a, Kristián Máthis^b,
František Chmelík^b, István Groma^a

^a*Eötvös Loránd University, Department of Materials Physics, 1117 Budapest, Pázmány Péter sétány 1/a. Hungary*

^b*Charles University, Faculty of Mathematics and Physics, Department of Physics of Materials, 121 16 Prague 2, Ke Karlovu 5, Czech Republic*

Abstract

PLEASE EDIT THIS .TEX!Metals usually deform irreversibly as a result of the motion of dislocations that are line-like defects in the crystal lattice. Compression experiments of micron-scale specimens^{1,2} as well as acoustic emission (AE) measurements performed on bulk samples^{3,4} revealed that the motion of dislocations resembles a stick-slip process. As a result, deformation proceeds in a series of unpredictable local strain bursts with a scale-free size distribution^{5,6}. Here we use a unique, highly sensitive experimental set-up, which allows us to detect the weak AE waves of dislocation slip during the compression of micron-sized Zn pillars. This opens up new vistas for studying the stop-and-go dislocation motion in detail and understanding the physical origin of AE events. Profound correlation is observed between the size of the deformation events and the total energy of the emitted signals that, as we conclude, are induced by the collective dissipative motion of dislocations.

*Corresponding author

Email address: `peter.ispanovity@ttk.elte.hu` (Péter Dusán Ispánovity)

We also show by statistical analyses of the acoustic event sequences that, despite of the fundamental differences in the deformation mechanism and the huge gap in the involved length and timescales, dislocation avalanches and earthquakes are essentially alike. Our experimental and computer simulation results not only unveil the complex spatiotemporal structure of strain bursts but also exhibit technological importance by unraveling the missing relationship between the properties of acoustic signals and the corresponding local deformation events.

Keywords: Crystal plasticity, dislocation avalanche, strain burst, micromechanics, acoustic emission

1 It was not until 1934 that the basic mechanism of irreversible (or plastic) de-
2 formation of metals was finally understood when Orowan, Taylor and Polányi
3 independently postulated the existence of a specific lattice defect^{7,8,9}. These
4 line-like defects, called dislocations, can move within the crystal lattice lead-
5 ing to the rearrangement of the atoms and, as a consequence, to the plas-
6 tic shear deformation of the crystal. Due to the huge dislocation content in
7 macroscopic metallic samples, their deformation usually appears as a smooth
8 process both in space and time. On microscopic scales, however, the picture
9 changes dramatically. Recent micromechanical experiments demonstrated
10 that when the sample diameter is below several couples of μm (depending on
11 the material), deformation becomes strongly heterogeneous. As pioneering
12 compression tests on Ni single crystal *micropillars* prepared using focused
13 ion beam (FIB) milling revealed, deformation is a sequence of sudden unpre-
14 dictable strain bursts that are localized to specific crystallographic planes of
15 the sample^{1,2}. During these intermittent bursts, dislocations locally disen-

16 tangle and move quickly for a short period and then form novel metastable
17 sub-structures at the end of an event. The burst sizes follow a scale-free
18 distribution that suggests an underlying self-organization of the dislocation
19 structure upon these plastic events^{5,6}.

20 A unique experimental method that is able to monitor this stochastic re-
21 sponse is the detection of AE waves. The principle of the emission of acoustic
22 waves in materials is analogous to earthquakes: Plastic deformation is caused
23 by the local rearrangement of dislocation lines in a crystal, a process that
24 is strongly dissipative and part of the released elastic energy escapes in the
25 form of elastic waves, that can be detected at the surface¹⁰. It was found that
26 in bulk ice single crystals the recorded AE signal is burst-like and the energy
27 associated with individual bursts follows a scale-free distribution^{3,4}. The
28 found power-law exponent is robust, typically not affected by deformation
29 mode, and for single crystals with hexagonal closed-packed (HCP) structure
30 it was measured to be $\tau_E = 1.5 \pm 0.1$ ¹¹. These kinds of measurements so
31 far have only been performed on bulk samples and it is believed – but not
32 yet demonstrated – that the AE waves are emitted from similar local strain
33 events that can be directly observed only for micron-scale objects.

34 One of the foremost achievements of this work is the realization of the
35 nontrivial task of detecting extremely weak AE waves which arise during
36 micropillar deformation. The main advantage of this approach is that, in
37 this case, AE sources are highly localized within a small micropillar volume
38 that prevents uneven attenuation of AE waves arising in different parts of
39 the specimen, this being inherent to bulk materials testing. Hence, plenty of
40 innate AE waves can be detected due to dislocation slip, which can, in turn,

41 provide interesting insights into the dynamics of plastic events. To achieve
42 this goal, the experimental set-up sketched in Fig. 1a was developed (see
43 Extended Data Fig. 1 for a photo). The device can be placed inside a scanning
44 electron microscope (SEM) that allows us to collect three different types of
45 information simultaneously during compression of the micropillars: (i) stress
46 and strain using a capacitive displacement sensor measuring the elongation
47 of a spring, (ii) acoustic signal from a piezoelectric transducer and (iii) visual
48 images using the electron beam of the SEM. The major difficulties for AE
49 detection in micropillars comprised the relatively low number of dislocations
50 involved in the slip process (compared to bulk materials testing) and various
51 sources of noise signals in the SEM chamber, mostly of electromagnetic origin.
52 For further details on the experimental set-up and remedies to these issues
53 see Methods.

54 Firstly, rectangular micropillars with a 3:1:1 aspect ratio and side lengths
55 of $d = 8 - 32 \mu\text{m}$ were prepared from a Zn single crystal oriented for single slip
56 (for more details on the sample see Methods). In Fig. 1b a micropillar during
57 the course of the experiment is shown. One can observe that dislocation
58 slip indeed takes place solely on the basal plane of the HCP lattice (see
59 also Supplementary Video 1). Since the crystal orientation in the pillar
60 remains the same throughout the entire loading (see Extended Data Fig. 2)
61 only dislocation glide is operative and deformation due to twinning can be
62 excluded.

63 Figure 1c plots the measured compressive stress σ as a function of time
64 t for the micropillar with $d = 32 \mu\text{m}$ shown in Fig. 1b (see also Supple-
65 mentary Video 1 for an in situ video of the compression). The pronounced,

66 close-to-vertical drops correspond to the strain bursts that lead to the sudden
67 elongation of the spring of the device. To analyse the spatial distribution of
68 a strain burst two consecutive SEM images taken before and after the stress
69 drop highlighted with grey color in Fig. 1c were compared with edge detec-
70 tion on the differential image and we concluded that deformation took place
71 solely in a thin slip band highlighted with red in Fig. 1b. During the compres-
72 sion, AE signal is also recorded that comprises numerous individual bursts
73 and their rate exhibits robust correlation with the stress drops (Fig. 1c). To
74 elaborate further on this finding Figs. 1d and 1e plot consecutively zoomed
75 parts of the stress-time curve shaded with grey colour. According to Fig. 1d
76 AE events can only be detected when plasticity occurs, that is, when the
77 stress-time curve deviates from the linear ramp-up characteristic of purely
78 elastic deformation. Interestingly, it is possible that several AE events cor-
79 respond to the same stress drop as also indicated by the event count number
80 (Fig. 1d). The reason for this is that the data acquisition rate differs consid-
81 erably between stress (200 Hz) and AE (2.5 MHz) measurements, the latter
82 allowing for a more detailed analysis. Figure 1e shows that the AE signal
83 consists of short ($\lesssim 100$ μ s) peaks standing out from the background noise.
84 We, thus, conclude that the AE events are indeed due to the dislocation ac-
85 tivity leading to plastic slip within the micropillar, however, the abundance
86 of AE events suggests that a measured stress drop is a result of complex
87 internal dynamics on timescales not accessible by stress measurements.

88 Origin of AE events

89 To quantify the correlation between plastic deformation and AE we now
90 turn to the statistical analyses of the measured data. In agreement with
91 studies on other single crystalline micropillars the distribution of the size of
92 the individual stress drops $\Delta\sigma$ follows a scale-free distribution with a cut-off
93 σ_0 : $P(\Delta\sigma) \propto \Delta\sigma^{-\tau_\sigma} \exp(-\Delta\sigma/\sigma_0)$ (Fig. 2a)^{5,6}. According to the inset, if the
94 axes are re-scaled with the cross section $A = d^2$ of the micropillars (that is,
95 force drop $\Delta F = A\Delta\sigma$ is considered as variable) the curves overlap and can
96 be fitted with a master function yielding $\tau_\sigma = 1.8 \pm 0.1$ and $F_0 = 1.5 \pm 0.1$ mN
97 for the exponent and the cutoff, respectively. Note that noise of the stress
98 measurement prohibits the reliable detection of drops below ~ 0.1 mN. The
99 distribution of the AE event energy E is characterized by another scale-free
100 distribution now without an apparent cut-off and dependence on pillar size:
101 $P(E) \propto E^{-\tau_E}$ (Fig. 2b) with $\tau_E = 1.7 \pm 0.1$. Note that the recorded AE
102 events were, in general, well-defined in time, with no significant effect of
103 signal overlapping or reflections (see Methods), as often observed in bulk
104 samples.

105 The facts that (i) stress drops $\Delta\sigma$ and AE energies E are detected in
106 a correlated manner, (ii) both obey a scale-free distribution and (iii) the
107 exponents are relatively close to each other suggest that there is a physical
108 relation between them. To shed light on such a link, Fig. 2c provides a scatter
109 plot of the *injected energy* E_{inj} and the detected AE energy E corresponding
110 to the individual stress drops (given that at least one AE event was detected
111 during the stress drop) for $d = 32$ μm pillars (for smaller pillar sizes see
112 Extended Data Fig. 3). The injected energy refers to the work done by

113 the compression device during a stress drop and is proportional with $E_{\text{inj}} \propto$
114 $(\sigma - \Delta\sigma/2)\Delta\sigma$ with σ being the applied stress at the onset of the event (see
115 ‘Energetic considerations’ in Methods for details and background discussion).
116 As said above, several AE events may be detected during a single drop.
117 In such cases the energies of the corresponding AE events are added. As
118 seen, there is a large scatter between $\Delta\sigma$ and E but, clearly, stress drops
119 with larger injected energy E_{inj} tend to emit AE signals with larger energies
120 also expressed by the Pearson correlation found to be 0.5 ± 0.1 . If one,
121 however, bins the data with respect to the injected energy a clear close-to-
122 linear dependence $E \propto E_{\text{inj}}$ is obtained between the two quantities. This
123 means that although a one-to-one correspondence between E and E_{inj} does
124 not exist, there is a linear relationship in the average sense that allows one
125 to obtain the distribution of the local energy release (that is proportional to
126 the plastic strain increment multiplied with the local stress during a local
127 deformation event) from the statistics of the AE events.

128 **Aftershock and foreshock statistics**

129 As mentioned above, AE signals emitted by local plastic deformation events
130 are similar to elastic waves caused by the seismic activity in the Earth’s
131 crust (although they differ in their amplitude and frequency spectra by sev-
132 eral orders of magnitude). To deepen the analogy, we now continue with the
133 analysis of AE signals that offer a much better time resolution than the stress
134 measurements. We intend to assess whether the AE bursts obey the three
135 ubiquitous fundamental scaling laws associated with earthquakes. (i) The
136 Gutenberg-Richter law¹² states that the probability density of an earthquake

137 with released energy E decays as a power-law¹³: $P(E) \propto E^{-w}$ with $w \approx 5/3$.
 138 (ii) According to the Omori law, the rate of aftershocks r_{as} after a main shock
 139 decays approximately inversely with the time t elapsed^{14,15}: $r_{\text{as}}(t) \propto t^{-p}$ with
 140 $p \approx 1$. (iii) The ‘aftershock productivity’ law in seismology concludes that
 141 main shocks with larger energy E_{ms} produce on average more aftershocks:
 142 $r_{\text{as}} \propto E_{\text{ms}}^{2\alpha/3}$ with $\alpha \approx 0.8$ found empirically¹⁶. The existence of scale in-
 143 variance through these power-law relationships has also been demonstrated
 144 in laboratory-scale compression experiments on porous bulk materials¹⁷ and
 145 rocks¹⁸.

146 It is found by our analysis that, despite the huge difference in spatial and
 147 temporal scales, the deformation mechanisms and the mode of loading, all
 148 three scaling laws are found to hold for micropillars, too. The Gutenberg-
 149 Richter law was demonstrated in Fig. 2b and Fig. 3a proves the Omori law
 150 for $d = 32 \mu\text{m}$ pillars. The line colours refer to the energy of the main shock,
 151 and it is clear that the rate indeed decays as a power-law with $p = 1.1 \pm 0.1$
 152 for approx. three decades and then saturates likely due to the onset of novel
 153 sequences. In accordance with the productivity law the rate is larger for
 154 larger main shocks and collapse can be obtained by re-scaling the rate with
 155 $E_{\text{ms}}^{0.5}$ (Fig. 3b), yielding $\alpha = 0.75$. As a further proof of equivalence, Fig. 3c
 156 plots the correspondent of the ‘inverse Omori law’ describing the power-law
 157 increase in the rate of foreshocks r_{fs} before a main shock¹⁹. (Extended Data
 158 Fig. 4 shows the corresponding figures for smaller pillars.) Previously, a sim-
 159 ilar analysis of AE on hexagonal ice at the bulk scale also showed increased
 160 triggering after large events, but the scale-free characteristics presented here
 161 were not possible to obtain, likely because of the relatively high level of

162 noise²⁰. It is also noted, that the difference between the foreshock and af-
 163 tershock rates is significantly smaller compared to that of earthquakes. It
 164 is speculated, that the difference is caused by the inambiguity in the de-
 165 termination of the main shock due to the noise present in the AE energy
 166 measurement.

167 The distribution of waiting times t_w between subsequent AE events, a key
 168 measure of temporal correlations and clustering in temporal processes^{21,22},
 169 was also analysed. For earthquakes a universal gamma distribution upon
 170 re-scaling with the seismic occurrence rate was reported²³. A similar distri-
 171 bution is found here (Fig. 3d): $P(t_w) = [At_w^{-(1-\gamma)} + B] \exp(-t_w/t_0)$, which
 172 can be interpreted as follows. The power-law decay for small ($\lesssim 0.1$ s) wait-
 173 ing times corresponds to the correlated temporal clusters originating from
 174 the same plastic event, often observed as a single stress drop. The exponent
 175 $1 - \gamma = 1.2 \pm 0.1$ coincides with the Omori exponent p within error margins,
 176 as expected. For larger times a plateau with an exponential cut-off is ob-
 177 served corresponding to a Poisson-like process of uncorrelated signals coming
 178 from different plastic events. To confirm this hypothesis we repeated the ex-
 179 periments for the $d = 8$ μm pillars with different platen velocities v_p (i.e.,
 180 deformation rates). Whereas the single event dynamics (power-law part) is
 181 unaffected by the velocity v_p (Fig. 3e), the collapse of the curves in the cut-off
 182 region after re-scaling the axes with the velocity v_p (Fig. 3f) yields $t_0 \propto v_p^{-1}$
 183 and $B \propto v_p$.

184 These results unveil an interesting two-level structure of plastic activity:
 185 accumulation of plastic strain is characterized by the intermittent appearance
 186 of uncorrelated slip bands. These strain bursts induce stress drops due to the

187 stiffness of the compression device. But AE measurements reveal that these
188 strain bursts themselves are characterized by a sequence of local events with
189 complex spatiotemporal dynamics. Firstly, Omori law and the waiting time
190 distributions report about scale-free temporal correlations. Secondly, since
191 strain increments during stress drops are localized in distinct slip bands (see
192 Supplementary video 1) and plastic activity was found to be responsible for
193 AE, one can conclude that the correlated AE events originate from a single
194 slip band, that is, they are not only temporally but also spatially correlated.
195 To quantify this observation the strain evolution between subsequent SEM
196 images during the *in situ* compression was analyzed in the Methods (see
197 section ‘Strain localization’) and we concluded that deformation during a
198 single stress drop is indeed highly localized and is typically concentrated in
199 one or sometimes few individual slip bands.

200 As seen in Fig. 2a the stress drop size distribution exhibits a cut-off, that
201 is, correlated consecutive triggering during a strain burst is limited. The
202 behaviour of the cut-off, thus, may shed light on the physics of the triggering
203 mechanisms. As it was mentioned, the cut-off in stress σ_0 decreases with in-
204 creasing pillar diameter d , but the cut-off in force $F_0 = d^2\sigma_0$ is independent
205 of d . According to Csikor *et al.* the physical origin of the cut-off is either
206 elastic coupling w the compression device (during an event the applied stress
207 drops that reduces the driving force of the event) or the strain hardening of
208 the material (during an event plastic deformation makes the material harder
209 so the driving force drops in a relative sense)⁶. From the comparison of the
210 behaviour of the cut-off with the predictions of Csikor *et al.* we conclude that
211 it is not the machine stiffness rather the local strain hardening in the acti-

212 vated slip band is responsible for stopping the consecutive triggering taking
213 place during a stress drop (see Methods for a detailed discussion).

214 Recently, Houdoux *et al.* investigated the plastic response of granular
215 systems that also showed remarkable analogy with earthquakes²⁴. They con-
216 cluded that in the triggering of subsequent events it is not the time but rather
217 the strain that matters. In our case, however, because the exponent $1 - \gamma$
218 is rather close to one, one cannot decide whether time (Fig. 3e) or strain
219 (Fig. 3f) matters in the triggering mechanism.

220 Numerical modelling

221 To provide a possible physical explanation for the experimentally observed
222 behaviour we conduct discrete dislocation dynamics (DDD) simulations of
223 parallel straight edge dislocations gliding on a single glide plane (see sketch
224 in Fig. 4a). Deformation of Zn micropillars is predominantly single slip,
225 yet, the computational model is a simplification of the realistic system as
226 it neglects, e.g., curvature and applies different boundary conditions (see
227 Methods for details). However, it captures properly the long-range stress
228 field of dislocations that was shown to play an essential role in the critical
229 behaviour of dislocations^{3,25}. Since no length-scale other than the average
230 dislocation spacing and the system size is present (due to the scale-free $1/r$ -
231 type dislocation interactions) dimensionless variables denoted with $(\cdot)'$ are
232 introduced hereafter (see Methods and Extended Data Table 1)^{26,27}.

233 A loading method analogous to the micropillar experiments is imple-
234 mented, i.e., a platen is moved with velocity v'_p and the load is transferred
235 to the system via a spring. As a result, dislocation avalanches appear as

236 stress drops here as well (Fig. 4b). During the avalanches, dislocations
237 move rapidly, and due to the overdamped dynamics assumed for dislocations
238 ($v' \propto F'$, where v' and F' is the velocity and the acting force for dislocations,
239 respectively) the elastic energy release rate reads as $\sum_i v_i'^2$, with the sum
240 performed over all dislocations. By thresholding this rate one can emulate
241 the sensitivity of the AE sensor and obtain simulated AE events as well as the
242 corresponding released energies (see Methods). Like in the experiments, the
243 simulated AE events show strong correlation with the stress drops (Fig. 4b,
244 Supplementary Videos 2, 3). It has been known that size distribution of dis-
245 location avalanches exhibits a different exponent in simulations compared to
246 the real samples^{25,28}, yet, the temporal clustering of the simulated AE events
247 shows very similar behaviour to experiments in terms of the correlation be-
248 tween injected energies and the AE energies (Fig. 4c), Omori law (Fig. 4d),
249 and waiting time distribution (Fig. 4e). We thus conclude, that the complex
250 dynamic behaviour observed in the experiments reported in this paper is
251 the result of the spatio-temporal correlations of the dislocations due to their
252 long-range elastic interactions and the lack of short-range mechanisms, such
253 as dislocation reactions.

254 **Outlook**

255 It has always been the fundamental assumption of AE experiments that the
256 parameters of the signals are characteristic of the local deformation process.
257 The experiments and simulations reported here prove this long-standing hy-
258 pothesis and reinforce that intermittency and scale-invariance characterizing
259 plastic deformation of HCP single crystals are related to the self-organized

260 critical (SOC) behaviour of dislocations. In addition, we showed that plastic
261 events, similarly to earthquakes, do not only exhibit spatial but also tempo-
262 ral clustering with long-range correlations, however, the involved length and
263 timescales are profoundly different, as summarized in Extended Data Table
264 2. This phenomenon also raises analogy with many other physical systems
265 exhibiting crackling noise²⁹. It is known, however, that SOC behaviour is
266 not ubiquitous in crystal plasticity, for instance, it is suppressed in materials
267 with FCC and BCC crystal structure and under multiple slip conditions likely
268 because of short-range interactions related to dislocation reactions and also
269 at high temperatures^{30,31,32}. Dedicated further experiments and modelling
270 based on the new methodologies of this paper are needed to study and under-
271 stand whether dislocation dynamics is altered under such circumstances in
272 terms of magnitude and spatiotemporal distribution of plastic fluctuations.

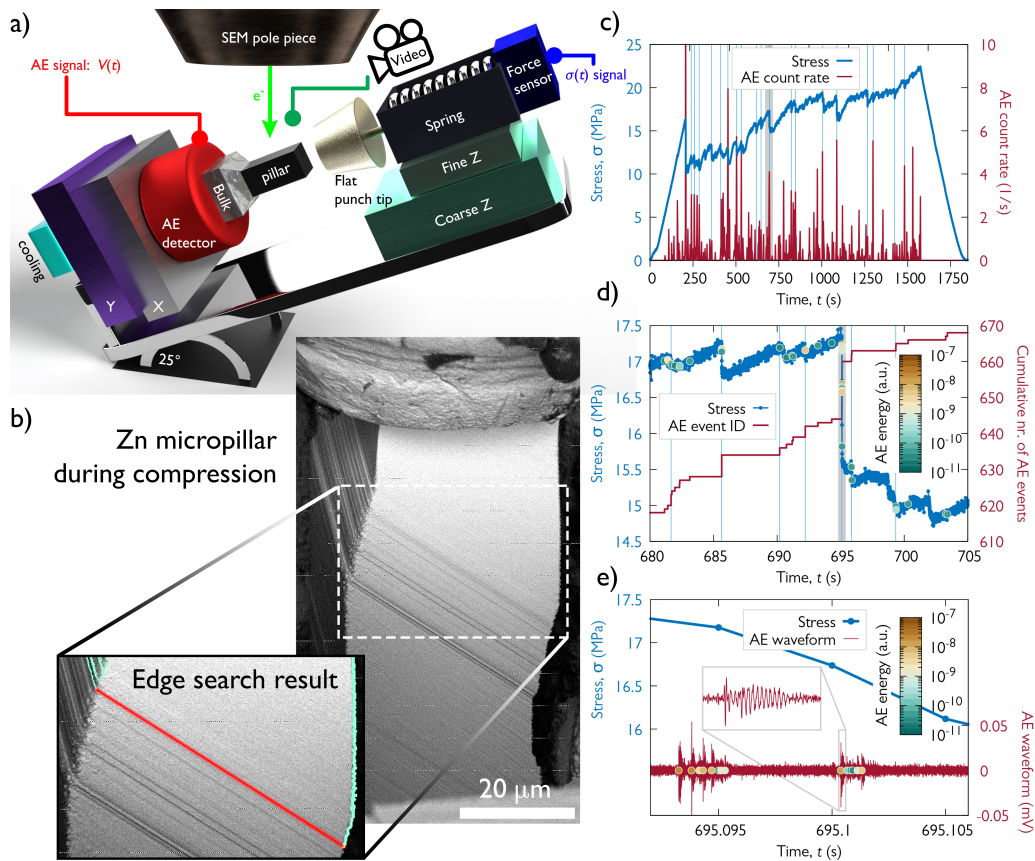


Figure 1: **Compression experiment of Zn micropillars oriented for single slip.** **a**, Sketch of the experimental set-up with a disproportionately large micropillar for clarity. **b**, Backscattered electron image of a $d = 32 \mu\text{m}$ micropillar during compression. The magnified image shows the slip band in red corresponding to the stress drop highlighted in grey in panels c and d. The location of the band was obtained by edge search on SEM images before and after the stress drop. **c**, Measured stress vs. time as well as the averaged rate (obtained by convolution with a Gaussian of 0.5 s width) of the detected individual AE bursts. The light blue vertical lines mark the stress drops larger than 1 MPa. **d**, Zoomed stress-time curve of the region shaded by grey in panel c. The coloured data points along the stress curve represent the individual AE events and their energies whereas the red curve shows the cumulative number of these events. The light blue vertical lines mark short periods with at least two AE events. **e**, Zoomed stress-time curve of the region shaded in grey in panel d and the detected AE waveform of the same interval. The inset shows the magnified view of a single event and coloured data points correspond to individual signals detected by thresholding the AE signal.

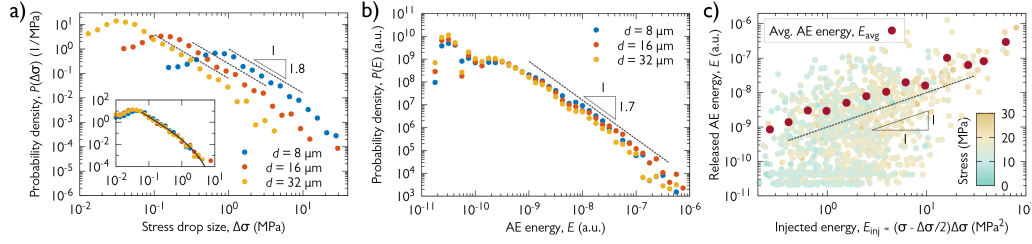


Figure 2: **Correlation between the stress drops and the acoustic signals.** **a**, Distribution of stress drop sizes $\Delta\sigma$ for different pillar diameters d . The probability density functions (PDFs) follow a power-law with exponent $\tau_\sigma = 1.8 \pm 0.1$. The inset shows the PDF as a function of the force drop $\Delta F = \Delta\sigma \cdot d^2$ with units in mN. The collapsed curves can be fit with a master function above the detection threshold and exhibit a cut-off at $F_0 = 1.5 \pm 0.1$ mN. **b**, Distribution of AE energies of individual signals detected at the sample surface. The curves are characterized by a power-law exponent $\tau_E = 1.7 \pm 0.1$ and do not exhibit an apparent cut-off and do not depend on the pillar diameter d . **c**, Scatter plot of the injected energies E_{inj} during stress drops of $d = 32 \mu\text{m}$ pillars and the corresponding summed released AE energies E . The color-scale refers to the actual stress at which the stress drop took place along the stress-time curve and do not show correlation with the injected energy. The red dots represent the average released energies E_{avg} obtained by averaging the datapoints for bins of logarithmically increasing width. The dashed line represents the $E \propto E_{\text{inj}}$ linear relationship. [szk: UPDATED!]

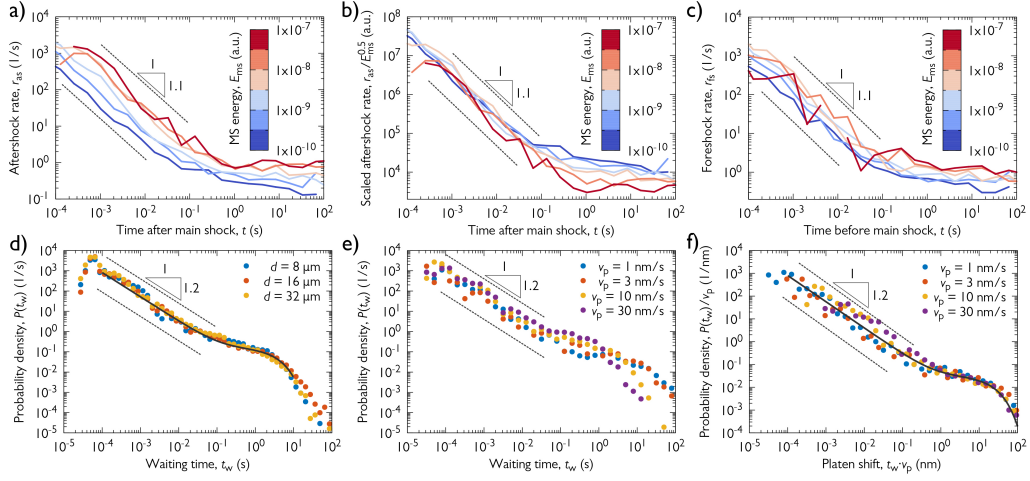


Figure 3: Temporal statistical analyses of AE events. **a**, The rate of aftershocks r_{as} after a main shock with an energy given by the colour for $d = 32 \mu\text{m}$ pillars (Omori law). **b**, Curves of panel a) divided with the square root of the main shock energy E_{ms} (aftershock productivity law). **c**, Rate of foreshocks r_{fs} before a main shock of energy given by the colours for $d = 32 \mu\text{m}$ pillars (inverse Omori law). **d**, PDF $P(t_w)$ of waiting times t_w between subsequent AE events for pillars of various sizes. **e**, $P(t_w)$ for $d = 8 \mu\text{m}$ pillars and different platen speeds v_p . **f**, $P(t_w)$ re-scaled with the platen velocity v_p . Note that the minimum t_w of $20 \mu\text{s}$, i.e., the minimum time between two subsequent AE events, is defined as one of the AE event individualization parameters (see Methods).

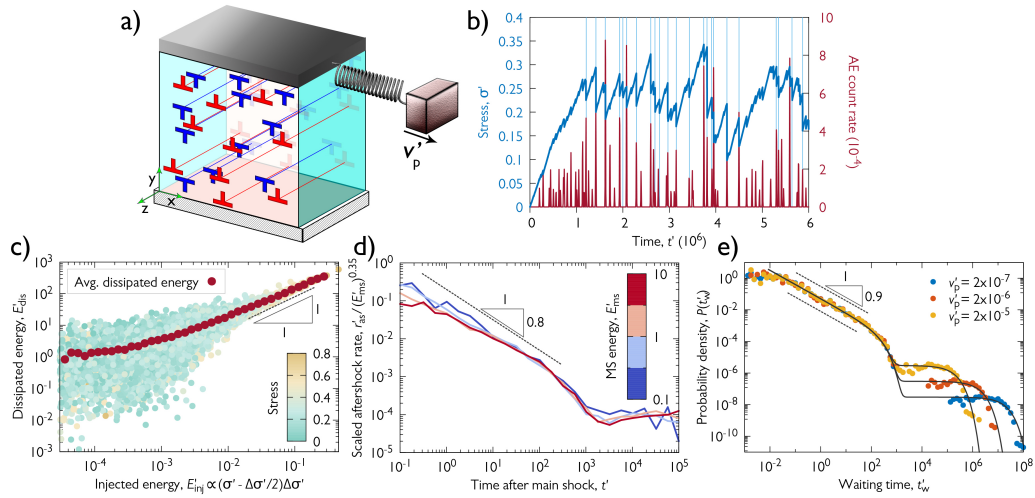


Figure 4: **DDD simulations.** **a**, Sketch of the simulation set-up. The system is infinite in direction z and periodic boundary conditions are applied in directions x and y . **b**, Stress vs. time curve as well as the averaged rate of the simulated individual AE bursts for a representative configuration. The light blue vertical lines show the stress drops larger than 0.02. **c**, Scatter plot of the injected energies during stress drops and the corresponding summed released AE energies for systems of $N = 1024$ dislocations, see caption of Fig. 2c for details. **d**, The rate of aftershocks r'_{as} scaled with $(E'_{ms})^{0.35}$ after a main shock with energy E'_{ms} given by the colour for $N = 1024$ dislocations (Omori and productivity laws). **e**, PDF $P(t'_w)$ for $N = 256$ dislocations and different platen speeds v'_p . [szk: UPDATED!]

273 **Methods**

274 **Sample preparation**

275 High purity single crystalline zinc heat treated at 100 °C for 4 h under at-
276 mospheric air, oriented for basal slip with side orientation corresponding to
277 the $\langle 2\bar{1}\bar{1}0 \rangle$ -type normal direction (Extended Data Fig. 2a) was mechanically
278 polished sequentially with SiC grinding paper and alumina suspension (down
279 to 1 μm). This was followed by a fast (10 s) electropolishing with Struers D2
280 solution at 20 V, 1 A. A sharp perpendicular edge was then created on the
281 bulk specimen by low energy Ar ion polishing (5 kV, 2 mA).

282 Experimental work including micropillar milling, EBSD measurements
283 and micromechanical testing was carried out inside the vacuum chamber of
284 an FEI Quanta 3D dual beam scanning electron microscope (SEM). Focused
285 ion beam (FIB) operating with Ga^+ ions was used to fabricate square-based
286 pillars of various sizes (8 μm : 13 pieces, 16 μm : 5 pieces and 32 μm : 4 pieces
287 with an approximate 3:1 aspect ratio of height to side), with final beam
288 conditions of 30 kV, 1 – 3 nA. In order to minimize Ga^+ ion contamination
289 on the surface and create practically non-tapered ($\leq 2.5^\circ$ between the side
290 and the loading axis) samples, the pillars were fabricated in a lathe milling
291 configuration³³. On the top of the pillars a thin (~ 350 nm) Pt cap was
292 deposited by FIB to act as hard buffer material between the pillars and the
293 flat punch tip and also to reduce ion contamination during FIB-milling.

294 Analytical methods

295 **Microstructure analysis**

296 For electron backscatter diffraction (EBSD) measurements, the Edax Hikari
297 camera was used with 1×1 binning, and the OIM Analysis v7 software pro-
298 vided the orientation results. Unit cell corresponding to the cross-sectional
299 side of the pillar can be seen in Extended Data Fig. 2. To calculate the
300 initial geometrically necessary dislocation (GND) density, a digital image
301 cross-correlation based technique called high (angular) resolution electron
302 backscatter diffraction (HR-EBSD) was applied³⁴. HR-EBSD determines lo-
303 cal strain and stress tensor components with the help of the raw diffraction
304 patterns. This method requires a reference diffraction pattern for the image
305 correlation, that is ideally captured in the strain-free state of the lattice. A
306 perfect reference pattern is often difficult to obtain experimentally, therefore
307 in our case a pattern with the presumably lowest stress is chosen, creating a
308 relative scale for the GND density. Diffraction patterns were recorded with
309 approx. 500×500 px² resolution from an area of 16.2×14.2 μm^2 with a step
310 size of 100 nm. The evaluation was carried out by BLGVantage CrossCourt
311 v4.2 software. 20 regions of interest (of 128×128 px² each, Extended Data
312 Fig. 5) were selected from each diffraction pattern to carry out the HR pro-
313 cessing with applied high and low pass filtering. All points in the map were
314 evaluated. The estimated average value of $\rho^{\text{GND}} = 1.2 \times 10^{13} \text{ m}^{-2}$ was mea-
315 sured on a surface prepared by the same FIB conditions (30 kV, 3 nA) as it
316 was used for the pillar fabrication prior to deformation. This value is close to
317 the detection limit of the GND density by HR-EBSD, hence it is concluded
318 that the sample preparation did not introduce a significant/measurable dis-

319 location content in the sample.

320 **X-ray line profile analysis**

321 Dislocation density characterization by X-ray diffraction measurements was
322 performed on the bulk Zn single crystal sample prior to the micropillar
323 fabrication. The X-ray line profiles of the $(10\bar{1}1)$ reflection were obtained
324 by a double-crystal diffractometer using Cu $K\alpha$ radiation (Extended Data
325 Fig. 6a). The experimental setup is of $\theta - 2\theta$ type, that consists of a high
326 intensity Rigaku RU-H3R rotating anode X-ray generator with a copper an-
327 ode, a monochromator that filters out the Cu $K\alpha_2$ component and redirects
328 the X-ray beam to the sample, and the Dectris MYTHEN 1D wide range
329 solid state X-ray detector that records the peak at a distance of 960 mm. We
330 also used a cylindrical vacuum chamber between the sample and the detec-
331 tor in order to increase the peak-to-background ratio. The quantification of
332 the total dislocation density was carried out by the variance method^{35,36} by
333 analyzing peak broadening based on the asymptotic behaviour of the second
334 order restricted moment:

$$M_2(q) = \frac{1}{\pi^2 \epsilon_F} q + \frac{\Lambda}{2\pi^2} \langle \rho \rangle \ln \frac{q}{q_0}, \quad (1)$$

335 where $q = 2(\sin \theta - \sin \theta_0)/\lambda$, λ corresponds to the wave length of the applied
336 X-rays, and θ and θ_0 are half of the diffraction and Bragg angles, respectively.
337 Parameter q corresponds to the distance from the peak center in reciprocal
338 space, q_0 is a constant depending on the dislocation-dislocation correlations,
339 ϵ_F is the coherent domain size, and $\langle \rho \rangle$ is the average dislocation density.
340 The value of Λ is commonly given as $\Lambda = \pi |\mathbf{g}|^2 |\mathbf{b}^2| C_{\mathbf{g}}/2$, where \mathbf{b} and \mathbf{g} are
341 the Burgers and diffraction vectors, respectively, and $C_{\mathbf{g}}$ is the diffraction

342 contrast factor that depends on the type of dislocations in the system and
343 on the relative geometrical position between the dislocation line direction \mathbf{l}
344 and the direction of \mathbf{g} ^{36,37}.

345 For this reason for the determination of the initial dislocation density one
346 has to make assumptions about the relative densities of dislocations of differ-
347 ent types. Since the energy of dislocations with Burgers vector lying in the
348 basal plane is lower compared to other types it is reasonable to assume that in
349 the original undeformed sample each slip system with a Burgers vector lying
350 in the basal plane is equally populated. To account for elastic anisotropy the
351 corresponding average Λ was determined numerically by the ANIZC program
352 (<http://metal.elte.hu/anizc/program-hexagonal.html>) and using the
353 elastic moduli of Zn, yielding $\Lambda = 0.506$ ^{38,39}.

354 As the coherent domain size is larger than $\sim 1 \mu\text{m}$, the first term in Eq. (1)
355 is negligible. As a result of the second term caused by the dislocations, M_2
356 versus $\ln(q)$ plot indeed becomes a straight line in the $q \rightarrow \infty$ asymptotic
357 regime, as shown in Extended Data Fig. 6b. From the fit a total dislocation
358 density of $\langle \rho \rangle^{\text{XRD}} = (1.5 \pm 0.1) \times 10^{14} \text{ m}^{-2}$ was obtained. As expected,
359 this value is higher than the GND density determined by the HR-EBSD
360 technique, therefore it can be assumed that the initial dislocation network
361 mostly consisted of statistically stored dislocations.

362 Micromechanical experiments

363 Testing device

364 Room temperature compression tests on the micropillars were carried out
365 in high vacuum mode inside the SEM chamber to allow *in situ* monitor-

366 ing of the deformation process and slip activity on the pillars' surface by
367 secondary and backscattered electrons. A custom-made nanoindenter^{40,41}
368 shown in Extended Data Fig. 1 was used without any load or strain feed-
369 back loop integrated. The precision of the indentation depth and load was
370 ~ 1 nm and ~ 1 μ N, respectively. The applied sampling rate was 200 Hz, while
371 platen velocity (if not stated otherwise) and spring constant were 10 nm/s
372 and 10 mN/ μ m, respectively. For a detailed description of the device, the
373 reader is referred to⁴⁰. Exemplary stress-strain curves are presented in Ex-
374 tended Data Fig. 7. The curves show the intermittent nature of plasticity in
375 micropillars and also provide evidence of the so-called plasticity size effect
376 ('smaller is harder').

377 **Cut-off analysis**

In this section background discussion is provided on the physics of the subse-
quent triggering taking place during an event cluster that is seen as a single
stress drop. During stress drops the driving force (that is, the applied stress
itself) gets smaller that is expected to reduce the probability of subsequent
triggering. In particular, the stress drop cannot be larger than the actual
stress itself, so, there is definitely a hard barrier related to the stress. How-
ever, according to Fig. 2a the stress drops get smaller for larger systems that
indicate that the stress may not be the limiting factor for avalanche propa-
gation. As shown by the inset, the cut-off in force F_0 is independent on the
specimen height $L = 3d$, which then also holds for the elongation increments
 $x_0 = F_0/k$, with k being the spring constant of the device. The effect of
machine stiffness on the avalanche cut-off was investigated by Csikor *et al.*⁶,

they found that the cut-off in *strain* obeys scaling:

$$\varepsilon_0 \propto \frac{bE}{L(\Theta + \Gamma)}, \quad (2)$$

where Θ and Γ are the strain hardening coefficient and the machine stiffness, respectively. In our case the machine stiffness is $\Gamma \approx k/L$, since the elastic deformation of the pillar is negligible compared to that of the spring. Hence, the cut-off in force reads as

$$F_0 = kx_0 = kL\varepsilon_0 \propto bE \frac{k}{\Theta + k/L}. \quad (3)$$

378 The finding that F_0 does not depend on L suggests that Θ is significantly
 379 larger than k/L . But if we look at the approximate values we see that
 380 $k/L \approx 100$ MPa (for a $32 \mu\text{m}$ pillar) and the average slope of the stress-
 381 strain curves is around 50 MPa. To overcome this apparent contradiction we
 382 consider the origin of Θ in the scaling relation above. During a stress drop not
 383 only the stress decreases but also the material gets harder (strain hardening),
 384 both processes act to cease the event. This is the reason the sum of Θ and Γ
 385 appear above in Eq. (2). In Ref.⁶ Θ was identified with the slope of the stress-
 386 strain curve. We believe, however, that this value is a local quantity and may
 387 differ from the global slope. During the compression of a pillar deformation
 388 proceeds in different shear bands. This can be envisaged as a weakest link
 389 process, that is, always the shear band with the lowest yield stress gets
 390 activated. After activation strain accumulates but the deformation stops
 391 and another shear band will get activated subsequently. This means that the
 392 yield stress of the activated shear band increases, that is, strain hardening
 393 takes place. This hardening coefficient of this local mechanism is nothing
 394 to do with the global coefficient, that also depends on the number of shear

bands and the distribution of the yield stresses of the shear bands. So, we argue, that the Θ in Eq. (2) may be significantly larger than the global strain hardening coefficient. This could explain why F_0 is independent of the system size and suggests that the local hardening mechanism is dominant in the avalanche cut-off over the stress decrease due to the applied spring. Whether local hardening is due to dislocation accumulation or dislocation starvation through the surface is an open question that future TEM investigations are expected to answer.

Edge detection

In order to investigate the spatial distribution of the plastic strain corresponding to individual stress drops, edge detection was performed sequentially on each SEM image of the $d = 32 \mu\text{m}$ micropillar shown in Fig. 1b. We aimed at detecting the vertical edge on the right side of the micropillar as it was characterized by a large difference in the intensity in the horizontal direction (due to the dark background). First, a vertical line was selected at the middle of the pillar as a reference. To detect the sudden change in intensity the pictures were then processed row by row starting from the reference line. If the drop in the intensity was larger than the given threshold, the point was marked as part of the edge. The horizontal coordinate x obtained at the height of z is denoted as $x_{\text{raw}}(z)$. The raw images were processed using the OpenCV package⁴².

The used backscattered electron detector introduced high intensity noise in the form of short horizontal lines with a width of few pixels, which needed to be filtered. Noise filtering was, thus, applied on $x_{\text{raw}}(z)$ with moving median smoothing. The window size was selected to be 7-7 pixels up and

420 down and if the current pixel along the x axis deviated for more than 2
421 μm , it was replaced by the median. The filtered curves are denoted as $x(z)$.
422 Supplementary Video 4 shows how the algorithm works during the course of
423 the experiment.

424 The time development of $x(z)$ is shown in Extended Data Fig. 8. The
425 base of the sample was moved to the origin and the results were rotated
426 by one degree clockwise. The white gaps represent strain bursts when large
427 plastic deformation occurs between consecutive images. The slip band can
428 be located by determining the end of the gap. As seen, the gaps end at
429 well-defined points, confirming that strain bursts take place within ‘thin’ slip
430 bands.

431 Based on Extended Data Fig. 8, the SEM images recorded before and
432 after the stress drop analysed in Figs. 1c-e were identified and the corre-
433 sponding edge shapes were denoted by purple and pink colours, respectively.
434 These SEM images are shown in Extended Data Figs. 9a-b. Although it is
435 barely seen by visual inspection, the quantified difference of the two images
436 $\Delta x_{\text{raw},t}(z, t) = x_{t+\Delta t}(z) - x_t(z)$ (Extended Data Figs. 9c) proves that defor-
437 mation took place along the slip plane at the height of $\sim 28 \mu\text{m}$ (as also seen
438 as horizontal grey line in Extended Data Fig. 8 and highlighted by a red line
439 along the corresponding basal plane in Fig. 1b).

440 **Strain localization**

441 In order to quantify how local deformation between two consecutive SEM
442 images was we started from the $\Delta x_{\text{raw}}(z)$ curves obtained in the previous
443 section. These curves were still rather noisy we, therefore, calculated the
444 moving average with a window size of 15 pixels and then applied a moving

445 median smoothing with a window size of 61 pixels. Finally, we made the
 446 curves monotonous, since slip in the opposite direction was not observed in
 447 the experiments. Three representative exemplary so obtained $\Delta x(z, t)$ curves
 448 can be seen below in the bottom row of Extended Data Fig. 10.

The obtained profiles usually exhibit a single slip band, but sometimes more than one step in the profile is seen. To quantify to what extent is the deformation localized we use the method of Ref.⁴³. Namely, we first note, that $\Delta x(z, t)$ is defined on an equidistant grid of the individual pixels of the SEM image. Let the discretized profile be denoted as Δx_i (for simplicity we omit the reference to time t). The local strain increment is then $\Delta \varepsilon_i^{\text{pl}} = \Delta x_{i+1} - \Delta x_i$. We now select an arbitrary point with index k along the height of the pillar and consider the typical distance of the plastic strain increments from this point as:

$$d_k = \frac{\sum_i \Delta \varepsilon_i^{\text{pl}} |k - i| \Delta z}{\sum_i \Delta \varepsilon_i^{\text{pl}}}, \quad (4)$$

where Δz is the pixel size of the SEM image. Then the minimum $d_{\min} = \min_k d_k$ is determined. For a homogeneous distribution of the plastic strain (i.e., $\Delta x(z)$ is a linear function) d_{\min} equals $L/4$, where L is the height of the micropillar. On the other hand, for a fully localized strain distribution (i.e., $\Delta x(z)$ is a step function) $d_{\min} = 0$ is obtained. The localization parameter is, therefore, defined as

$$\eta = 1 - \frac{4}{L} d_{\min}. \quad (5)$$

449 Consequently, $\eta = 0$ signals a homogeneous deformation, whereas $\eta = 1$ is
 450 characteristic of deformation fully localized in a single slip band.

451 Figure 10 summarizes the analysis performed on those consecutive images,
 452 where the event size defined as $\Delta x(L) - \Delta x(0)$ (that is, the displacement

453 between the top and bottom of the pillar) was larger than $0.02 \mu\text{m}$ [pi: ???].
454 As seen the localization η is typically between 0.5 and 1 and its average is
455 $\langle \eta \rangle = 0.74$ [pi: ???]. This high value of η clearly shows that plastic strain
456 increments are quite localized. The fact that the values are smaller than 1
457 are likely due to the numerical noise present in the edge detection and that
458 between two consecutive SEM images (that takes around 0.25 s) more than
459 one events can take place.

460 So, based on this analysis we conclude that the plastic strain increments
461 are highly localized, typically concentrating in a single slip band. Since
462 the AE events are observed during the accumulation of plastic strain, it is
463 natural to assume that a cascade of events correlated in time originate from
464 the same (typically one, sometimes few) slip band. This means these events
465 are not only correlated in time, but also in space. More details on the spatial
466 correlations are not possible to obtain with the present experimental methods
467 due to the small volume of the specimen.

468 AE measurements

469 Detecting AE signals

470 By definition, acoustic emissions are transient elastic waves generated in ma-
471 terials due to sudden localized and irreversible structure changes⁴⁴. The
472 detection of AE waves is based on its physical nature – when the material
473 is subjected to external loading, released energy forms stress pulses propa-
474 gating through the material as transient elastic waves. The wave component
475 perpendicular to the surface is detected typically by a piezoelectric trans-
476 ducer (attached directly to the specimen surface), which converts recorded

477 displacements into an electrical signal.

478 The nanoindenter device was equipped with a Physical Acoustics Corpo-
479 ration (PAC) WS α wide-band (100-1000 kHz) AE sensor, which showed a
480 superior combination of frequency and sensitivity characteristics over other
481 tested sensors (PAC Micro30S, PAC F15I-AST). The Zn single-crystal (with
482 FIB-milled micropillars on the surface) was attached to the transducer over
483 a layer of vacuum grease to ensure effective acoustic coupling. Mechanical
484 bonding ('clipping') was carried out by means of a thin metallic strip bent
485 over the sample and fixed at both ends to the device, ensuring a constant
486 contact pressure during the compression tests. The recorded signal was am-
487 plified using the Vallen AEP5 pre-amplifier set to 40 dB_{AE}. Data acquisition
488 and processing were performed using the computer-controlled Vallen AMSY-
489 6 system. Data acquisition was carried out in continuous data streaming
490 mode, i.e., the whole raw acoustic data sets were recorded for further post-
491 processing at a sampling rate of 2.5 MHz.

492 **Identification of AE events**

493 To individualize the AE events, an in-house script implemented in Matlab
494 was used. The threshold voltage was set to $V_{\text{th}} = 0.01$ mV, this value being
495 slightly above the background noise. The hit definition time (HDT), i.e., the
496 minimum period between two subsequent AE events, used for the separation
497 of events was 20 μs .

498 In Extended Data Fig. 11 various parameters of a representative event
499 related to the AE measurements are defined. The original AE waveform $V(t)$
500 is plotted in the inset as a function of time t . The AE event energy is defined

501 as the area under the squared signal amplitude curve:

$$E = \int_{t_b}^{t_e} V^2(t)dt, \quad (6)$$

502 where t_b and t_e denote the beginning and end of the event, respectively (that
503 is, E is the extent of the area shaded in blue in Extended Data Fig. 11).

504 The AE counts are defined as the number of data points (in absolute values)
505 crossing the threshold level V_{th} . The duration of one AE event is defined as
506 the time between the first and the last AE count in that event.

507 **Data validation**

508 The common source of both load drops and AE events in the tested mi-
509 cropillars are dislocation avalanches in the basal plane. In order to exclude
510 any other external effects that might lead to the generation of AE events,
511 additional aspects of the AE measurement had to be addressed: (i) friction
512 between the indenter's flat diamond tip and the top of the pillars and (ii)
513 possible noise or vibrations from external sources and the nanotesting device
514 itself.

515 To address point (i) we investigated six micropillars with identical geom-
516 etry, fabricated by three different methods for this purpose. Two pillars were
517 prepared with Pt coating, two with C coating and two pillars without any
518 coating on top. Although three materials with different friction properties
519 were used, the analysis produced practically identical results with respect
520 to the AE events and strain bursts. To avoid the presence of any spurious
521 extrinsic vibrations considered within point (ii), three further compression
522 tests were carried out where a special tip suspension was applied – another
523 elastic part (a piece of rubber) was added to the device to isolate possible

524 vibrations and noises from external sources. Just as in the previous case (i),
 525 this analysis demonstrated that there were no observable differences in the
 526 AE data compared to the tests without this additional suspension.

527 **The overlapping of AE events**

528 Assuming that the AE events originate from individual well-defined plastic
 529 events (i.e., dislocation avalanches related to stress drops) and there are no
 530 significant scattering and echoing mechanisms during the wave propagation,
 531 one may expect an exponential decay of the waveform resulting from intrinsic
 532 absorption^{45,46}. In that case, the relationship between the maximum squared
 533 amplitude

$$A^2 = \max_{t \in [t_b, t_e]} V^2(t), \quad (7)$$

534 and the duration $T = t_e - t_b$ could be written as

$$A^2(T) = V_{\text{th}}^2 \exp\left(\frac{T}{\tau}\right), \quad (8)$$

535 where τ is a timescale characterizing the rate of absorption⁴⁶. This rela-
 536 tion was fitted to all data points that were detected under the same noise
 537 conditions. This set of data contained more than 13,000 events from the
 538 compression tests on Zn pillars with various dimension. The data trends and
 539 exponential fits shown in Extended Data Fig. 12 prove the validity of relation
 540 (8); thus, we concluded that the majority of detected events are due to short
 541 pulse-like events at the source attenuated only by intrinsic absorption, while
 542 recording of wave reflections and overlapping events is not common with the
 543 AE event individualization parameters used in this study (see above). It is
 544 also noted, that the fitted value of $\tau = 45 \mu\text{s}$ is below the typical time-scales
 545 characteristic of the Omori-law and waiting time distributions in Fig. 3.

546 **Rates of aftershocks and foreshocks**

547 Large AE events, similarly to earthquakes, are usually followed by several
548 aftershocks. To quantify the rate of these aftershocks the following procedure
549 was implemented. First, we select an energy interval $[E_{\text{ms}} - \Delta E/2, E_{\text{ms}} +$
550 $\Delta E/2]$ and consider only AE events with energies falling in this given bin.
551 These will be the main shocks with energy E_{ms} . The sequence of events
552 (aftershocks) corresponding to each main shock lasts until an event with
553 energy falling in this or larger bin takes place. The time after the main shock
554 t is binned logarithmically, and the AE events in the sequence following the
555 main shock falling in each bin are counted, and then repeated for all main
556 shocks with energy E_{ms} . To obtain the rate of the aftershocks $r_{\text{as}}(t)$ the
557 number of events in the time bin around t is normalized with the bin width
558 and also with the number of sequences that reached the given length t . The
559 obtained $r_{\text{as}}(t)$ curves for $d = 32 \mu\text{m}$ pillars are plotted in Figs. 3a-b. The
560 corresponding figures for smaller micropillars are shown in Extended Data
561 Figs. 4a-d.

562 In the case of foreshock rates r_{fs} the same procedure was adopted and
563 inverted in time to investigate sequences before main shocks. The obtained
564 rates for $d = 32 \mu\text{m}$ pillars are seen in Fig. 3c and for smaller ones in Extended
565 Data Figs. 4e-f.

566 **Waiting time of AE events**

567 The waiting time distributions of Figs. 3d-f are obtained as follows. The
568 identification of the individual AE events described above in section ‘Identi-
569 fication of AE events’ yields the time t_i of each event. The waiting time is
570 then simply $t_{\text{w},i} = t_{i+1} - t_i$, and the distribution of these values is computed.

571 Since only those AE events can be detected that rise above the back-
 572 ground noise, it is important to check the role of thresholding in the obtained
 573 distributions. To this end, the procedure described above was repeated after
 574 considering only events with energies E larger than a threshold E_{th} . Ac-
 575 cording to Extended Data Fig. 13a they only differ in the exponential tail
 576 characterized by parameter t_0 related to the average time between subse-
 577 quent uncorrelated event clusters. As seen, increase of E_{th} leads to fewer
 578 detected events and, thus, an increased t_0 . To prove that thresholding does
 579 not influence the conclusions of the paper, in Extended Data Fig. 13b the
 580 distributions were re-scaled with the average waiting time $\langle t_w \rangle$ correspond-
 581 ing to the given threshold E_{th} . The obtained collapse of the curves means
 582 that $t_0 \propto \langle t_w \rangle$ similarly to what was obtained in the case of different platen
 583 velocities v_p (Figs. 3e-f), and it proves scale-invariance of the AE events.

584 **Energetic considerations**

585 In this section background discussion is provided for the comparison of the
 586 energies of strain bursts and the corresponding AE events with an emphasis
 587 on the analogies with earthquakes. We start by noticing that there are three
 588 relevant energy quantities one may look at. The first one we call *injected*
 589 *energy* and is the work done by the compression device during an event:

$$E_{\text{inj}} = \bar{F} \Delta s \approx \frac{\sigma_0 + \sigma_1}{2} A \Delta s, \quad (9)$$

590 where \bar{F} is the average force exerted by the device, Δs is the displacement
 591 of the punch tip, σ_0 and σ_1 are the stresses before and after the event and A
 592 stands for the cross-section of the sample. This expression is equivalent to
 593 Eq. (3.14) in the review article on earthquake physics⁴⁷ where it is termed

594 *potential energy*. If we assume a quick event with a stress drop of $\Delta\sigma =$
 595 $\sigma_0 - \sigma_1$, then

$$E_{\text{inj}} \approx \frac{A}{k}(\sigma_0 - \Delta\sigma/2)\Delta\sigma \propto (\sigma_0 - \Delta\sigma/2)\Delta\sigma, \quad (10)$$

596 where k is the stiffness of the device.

597 This work E_{inj} is not necessarily equal with the dissipated energy, since
 598 the energy stored as elastic energy may change during an event. The second
 599 relevant energetic quantity is, therefore, the *dissipated energy* that actually
 600 equals the change of the elastic stored energy of the system (in this sense,
 601 the external work initially increases the elastic energy of the sample part of
 602 which then gets released due to plastic processes). Assuming a $v \propto \sigma$ linear
 603 relationship between the local stress and the drag acting on dislocations, the
 604 change in the elastic energy can be written in the form:

$$E_{\text{dis}} \propto \sum_{i=1}^N \int_{t_0}^{t_1} v_i^2 l_i dt, \quad (11)$$

605 where t_0 and t_1 mark the beginning and the end of an event, respectively,
 606 and v_i and l_i are the velocity and length of the i th dislocation or dislocation
 607 segment, respectively. This formula is the analogue of Eq. (3.12) of⁴⁷, that
 608 is termed *radiated energy* for earthquakes.

609 The dissipated energy may create, e.g., heat or elastic waves. With an
 610 acoustic transducer some part of the energy released in the form of elastic
 611 waves can be detected [denoted by E in Eq. (6)]. Here we arrive at the issue
 612 of efficiency. It is, of course, not known what portion of the dissipated energy
 613 gets converted into elastic waves and what fraction of it can be measured at
 614 the surface. Here we make the simplest and most straightforward assumption

615 that this ratio does not depend on the energy of the event, so, the measured
616 AE energies are representative of the released energy: $E \propto E_{\text{dis}}$. We note
617 that our situation is somewhat simpler than earthquakes since here only one
618 type of deformation is active contrary to earthquakes where rupture and
619 thermally activated processes may also play a role.

620 Concerning the relationship between E_{inj} and E_{dis} the natural assumption
621 is again a linear dependency in the average sense. This idea, however, can be
622 tested by the DDD simulations as there we have direct access to microstruc-
623 tural data, i.e., dislocation positions and velocities. It is evident from Fig. 4c
624 in the main text that $E_{\text{dis}} \propto E_{\text{inj}}$ holds.

625 In the case of experiments only the injected energy E_{inj} and the detected
626 acoustic energy E can be measured. In Fig. ?? we plot the two quantities
627 against each other for individual events. As seen, in this case a linear rela-
628 tionship between E_{inj} and E is obtained that seem to match the assumptions
629 mentioned above.

630 Simulations

631 Discrete dislocation dynamics

632 The model to be investigated is one of the simplest discrete dislocation sys-
633 tems that still incorporates the following fundamental physical properties of
634 dislocations:

- 635 • $1/r$ -type long-range interactions between dislocation lines.
- 636 • Non-conservative motion of dislocations due to the strong phonon drag.

637 • Geometrically constrained motion of dislocation lines, since at low tem-
638 peratures they can only glide in certain planes (called glide planes).
639 As a result, the system cannot reach a global energy minimum state,
640 rather, it gets trapped in a meta-stable configuration.

641 The system consists of straight edge dislocations parallel with the z axis,
642 and their slip planes are parallel with the xz plane (single slip). Since the
643 system is translationally invariant along the z axis it can be considered two-
644 dimensional (2D) and it is sufficient to track the motion of dislocations in the
645 xy plane. In this set-up the Burgers vector points in the x direction and, thus,
646 reads as $\mathbf{b} = s(b, 0)$, where $s \in \{+1, -1\}$ is the *sign* of the dislocation, that
647 can be understood as some kind of charge. Extended Data Fig. 14a shows an
648 example of such a 2D dislocation configuration. The colours of dislocations
649 represent their sign and the background colour refers to the local shear stress
650 within the embedding elastic medium.

651 Because of the strong dissipation due to phonon drag, the motion of
652 dislocations is assumed to be overdamped, that is, the force acting on a
653 dislocation of unit length is proportional to its velocity. If the system consists
654 of N dislocations and $\mathbf{r}_i = (x_i, y_i)$ denotes the position of the i th ($i =$
655 $1, \dots, N$) dislocation then the equation of motion reads as

$$\dot{x}_i = Ms_i b \left[\sum_{j=1; j \neq i}^N s_j \sigma_{\text{ind}}(\mathbf{r}_i - \mathbf{r}_j) + \sigma \right], \quad (12)$$

$$\dot{y}_i = 0. \quad (13)$$

656 Here M is the dislocation mobility, σ is the externally applied shear stress
657 and σ_{ind} is the shear stress field generated by individual dislocations. For the

658 latter the solution corresponding to isotropic continua is used⁴⁸:

$$\sigma_{\text{ind}}(\mathbf{r}) = \frac{\mu b}{2\pi(1-\nu)} \frac{x(x^2 - y^2)}{(x^2 + y^2)^2}, \quad (14)$$

659 where μ and ν denotes the shear modulus and the Poisson number, respec-
660 tively. Dislocations are arranged in a square-shaped simulation area and
661 periodic boundary conditions (PBC) are applied. The emerging image dis-
662 locations alter the stress field of Eq. (14) (that corresponds to an infinite
663 medium), which can be obtained using a Fourier method (see Extended Data
664 Fig. 14b)⁴⁹. The equations of motion (12,13) are solved using a fully implicit
665 scheme that makes usage of annihilation unnecessary, so, it is not imple-
666 mented⁵⁰.

667 With the application of the PBCs surface effects that may be important
668 for small scale samples are neglected in the simulations. Indeed, in nanopil-
669 lars it was found that exhaustion hardening⁵¹ as well as dislocation source
670 truncation⁵² represent key physics in the plastic deformation that lead to
671 size-effects. These single-dislocation properties are important at scales com-
672 parable or smaller than the average dislocation spacing, in our case being
673 around $\rho^{-0.5} \approx 0.1 \mu\text{m}$. In our experiments the micropillars are rather large
674 ($8 - 32 \mu\text{m}$) compared to previous studies, and at this scale collective dis-
675 location dynamics is expected to dominate plasticity and boundary effects
676 can be neglected. This explains our choice for the PBCs that allowed us to
677 concentrate on collective dislocation phenomena. It is also noted, that in
678 experiments plastic deformation leads to the shape change of the sample and
679 may cause some lattice rotation. These effects are not expected to have a
680 significant role in the observed dynamics and are neglected in the simulations.

681 One of the main advantages of the model system introduced is that the

682 dislocation interactions exhibit a $1/r$ -type decay. This means that apart from
683 the average dislocation spacing (being equal to $\rho^{-0.5}$, where ρ is the total dis-
684 location density) no additional length scales appear in the model. One may,
685 thus, introduce dimensionless variables by measuring length, stress, strain
686 and time in units summarized in Extended Data Table 1, where notation
687 $G = \mu/[2\pi(1 - \nu)]$ is introduced.

688 Initially, an equal number of positive and negative sign dislocations are
689 positioned randomly in the square-shaped simulation area with uniform dis-
690 tribution. At zero applied stress the system is first let to evolve into a relaxed
691 equilibrium configuration. After that the applied shear stress is increased us-
692 ing a protocol emulating the experimental set-up of micropillar compression.
693 Namely, the applied stress is computed at every time step according to

$$\sigma' = r'(v_p' t' - \varepsilon' L'), \quad (15)$$

694 where v_p' is the platen velocity (see Fig. 4a), t' is the simulation time, r' is
695 a constant characterizing the strength of the spring connecting the platen
696 and the dislocation system, and ε' is the accumulated plastic shear strain
697 computed as:

$$\varepsilon'(t') = \sum_{i=1}^N s_i [x_i'(t') - x_i'(0)]. \quad (16)$$

698 In the simulations $r' = 1/32$ was used and the platen velocity (if not stated
699 otherwise) was set to $v_p' = 1.6 \times 10^{-4}$.

700 **Event detection**

701 The overdamped dynamics used in Eqs. (12,13) reflects the fact that dis-
702 location motion is a highly dissipative process during which stored elastic

703 energy E'_{el} of the embedding crystal is transformed into other types of en-
 704 ergies (e.g., heat or elastic waves). This energy dissipation rate r'_{en} can be
 705 obtained as

$$r'_{\text{en}} = -\dot{E}'_{\text{el}} = \sum_{i=1}^N (v'_i)^2, \quad (17)$$

706 where $v'_i = \dot{x}'_i$ is the velocity of the i th dislocation.

707 Stress drop detection is based on the finding that in active periods the
 708 dissipation rate r'_{en} increases several orders of magnitudes as demonstrated
 709 on an exemplary event in Extended Data Fig. 15. To obtain the beginning
 710 t'_b and end t'_e of the event a threshold of $r'_{\text{th}} = 5 \cdot 10^{-6}$ was used for the
 711 dissipation rate as demonstrated in Extended Data Fig. 15. The size of the
 712 stress drop then follows as $\Delta\sigma' = \sigma'(t'_e) - \sigma'(t'_b)$.

713 As seen in Extended Data Fig. 15, a plastic event exhibits a fine struc-
 714 ture with many peaks in the dissipation rate r'_{en} . In order to emulate an
 715 AE detector, an additional threshold $r'_{\text{th,AE}}$ is defined that characterises the
 716 sensitivity of the detector: whenever $r'_{\text{en}} > r'_{\text{th,AE}}$ the detector is able to mea-
 717 sure the dissipation rate. With this, emulated AE events can be defined as
 718 demonstrated in the inset of Extended Data Fig. 15. The threshold $r'_{\text{th,AE}}$
 719 breaks up the signal in individual AE events, with their energy E' being the
 720 size of the area shaded alternately in blue and red colour. Data processing
 721 was carried out with the utilization of the NumPy library⁵³.

722 From the list of stress drops and AE events the AE count rate, the cor-
 723 relation between stress drops and AE energies, the aftershock rates and the
 724 waiting time distributions in Figs. 4b-e were determined with the same pro-
 725 cedure as for experiments. The role of the threshold $r'_{\text{th,AE}}$ used to model
 726 AE detector sensitivity was also investigated. According to Extended Data

727 Fig. 16 the Omori law as well as the productivity law are recovered in a
728 wide range of thresholds, however, small thresholds lead to the coalescence
729 of events leading to a deviation from the power-law behaviour for small times
730 t' . In Figs. 4d-e $r'_{\text{th,AE}} = 3.16$ was used for AE individualization.

731 **Data availability**

732 All data are available in the main Article and Methods, or from the corre-
733 sponding author upon reasonable request.

734 **Code availability**

735 The numerical methodology used in this study is described in Methods and
736 the source code is available at:
737 <https://github.com/pgabor/dislocation-avalanches-earthquakes>.

738 **Acknowledgements**

739 The work was performed within the ELTE Institutional Excellence Program
740 (TKP2020-IKA-05) supported by the Hungarian Ministry of Human Capac-
741 ities. P.D.I, D.U., G.P., D.T. and I.G. acknowledge support by the National
742 Research, Development and Innovation Fund of Hungary (contract numbers:
743 NKFIH-K-119561 and NKFIH-FK-138975). D.U. was also supported by the
744 ÚNKP-20-3 New National Excellence Program of the Ministry for Innova-
745 tion and Technology from the source of the National Research, Development
746 and Innovation Fund. G. P. was also supported by the ÚNKP-21-3 New
747 National Excellence Program of the Ministry for Innovation and Technology
748 from the source of the National Research, Development and Innovation Fund.

749 M.K. and F.C. received financial support from the Czech Science Foundation,
750 Grant No. 19-22604S.

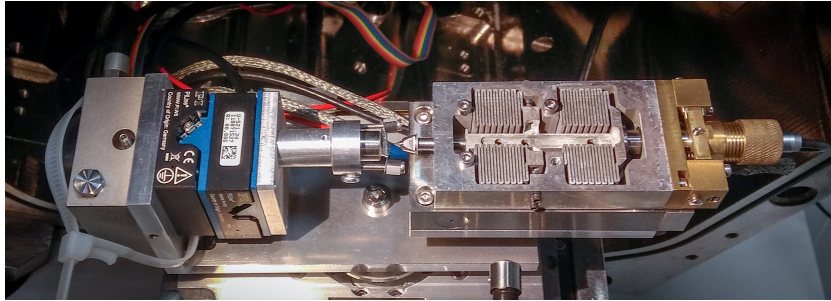
751 **Author Contributions**

752 P.D.I. designed the research and supervised the project. P.D.I., D.U., Z.D.,
753 D.T. and I.G. designed and developed the microdeformation stage. D.U. per-
754 formed micropillar fabrication and compression experiments as well as EBSD
755 and X-ray measurements. D.U., M.K., K.M. and F.C. performed the AE
756 measurements. S.K. assisted with the sample preparation and analysis.
757 P.D.I., D.U. and S.K. analysed the experimental data. I.G. assisted at every
758 experimental measurement. G.P. developed and performed the simulations
759 and performed the slip band analysis. P.D.I., D.U., G.P., S.K., M.K. and
760 K.M. wrote the paper, with contributions from all authors.

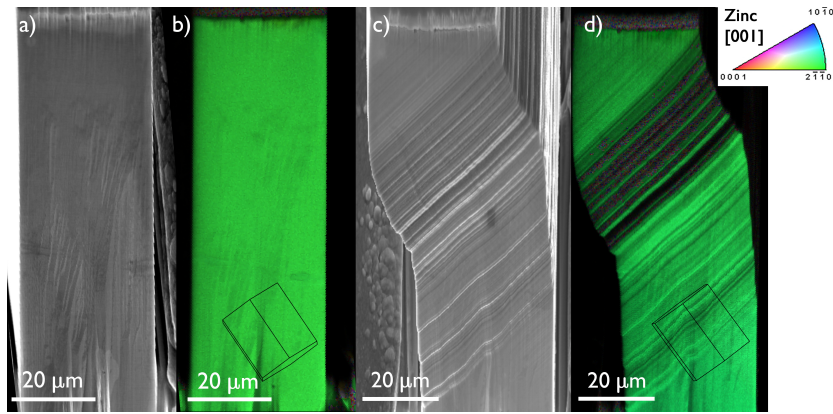
761 **Competing Interests Statement**

762 The authors declare no competing interests.

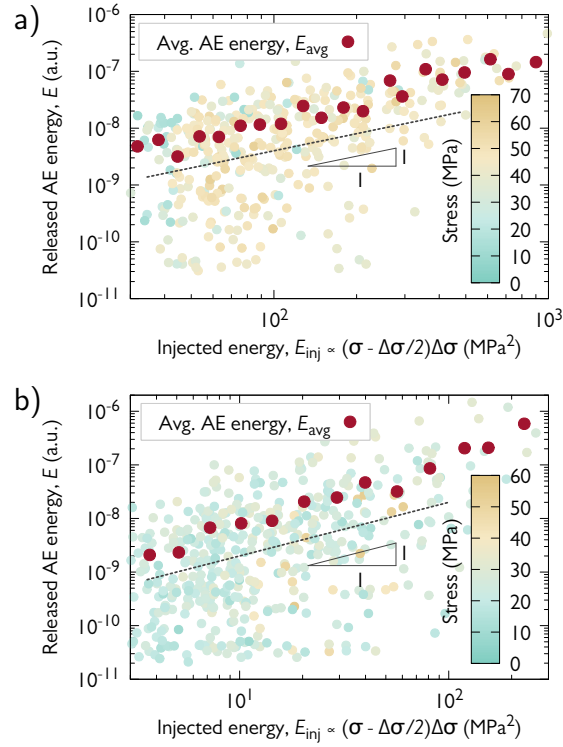
763 Extended data figures and tables



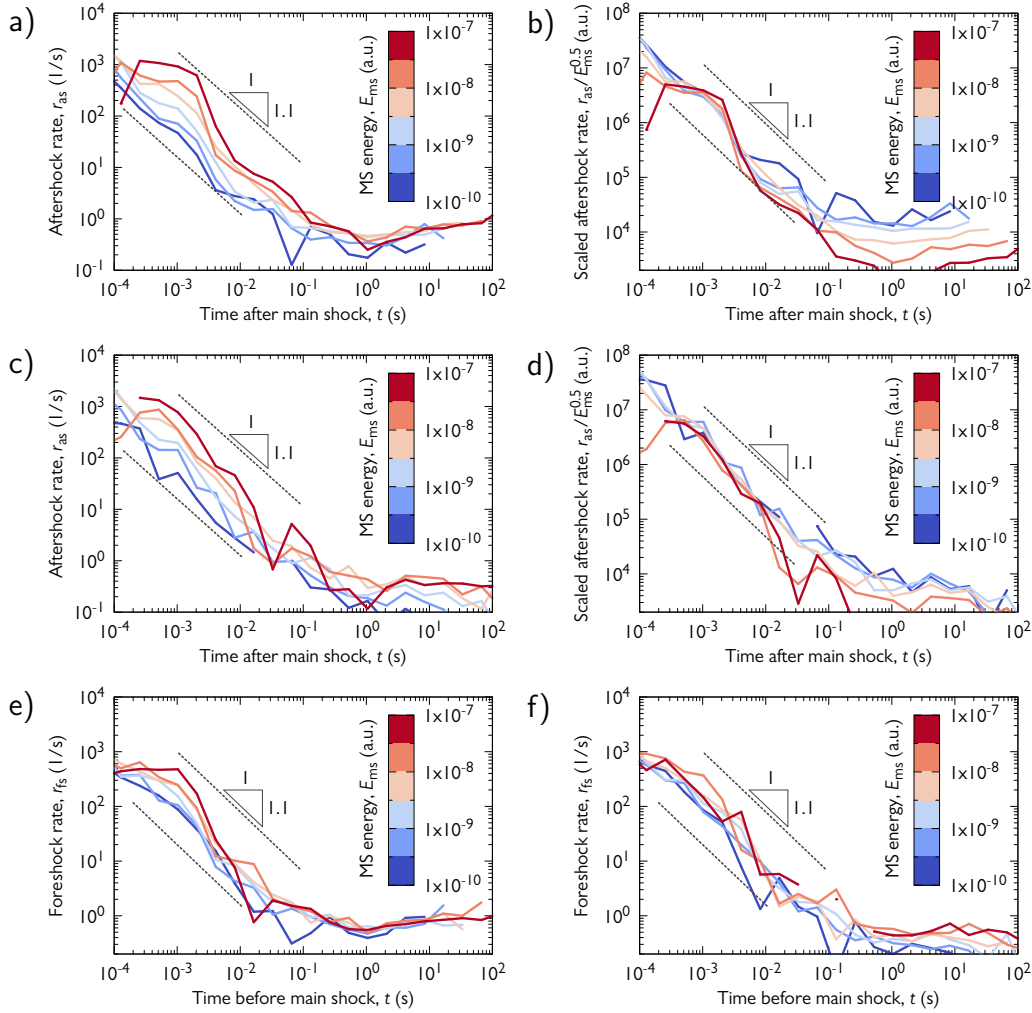
Extended Data Figure 1: In-house developed *in situ* nanoindentation set-up.



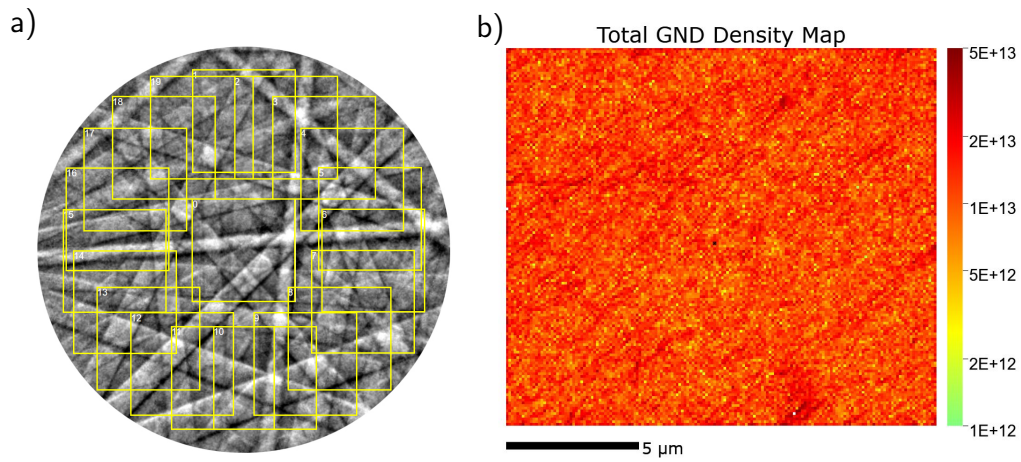
Extended Data Figure 2: **SEM imaging of the micropillars.** **a, c,** Secondary electron image of the same pillar in a tilt-corrected (70°) view before and after deformation. Note the uni-directional parallel slip bands in the deformed pillar. **b, d,** EBSD orientation map measured before and after compression of a Zn micropillar. The uniform color confirms single crystal structure both before and after the deformation. The orientation of the unit cell is also shown proving that the slip bands are parallel with the basal plane of the crystal.



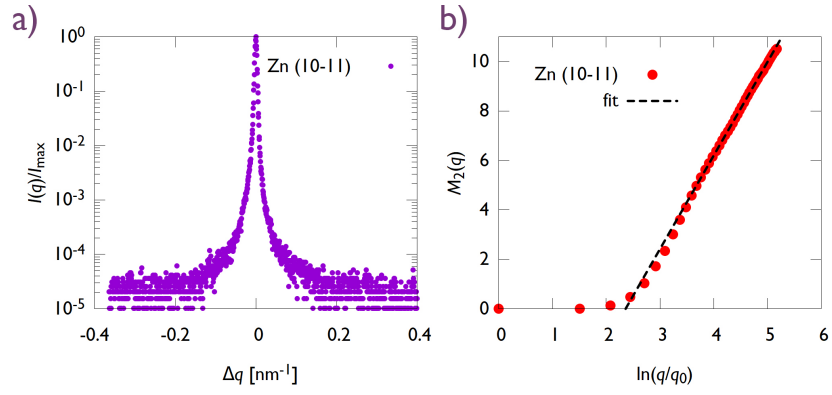
Extended Data Figure 3: **Correlation between stress drops and released AE energy.** **a**, Equivalent figure to that of Fig. 2c for $d = 8 \mu\text{m}$ micropillars. **b**, Equivalent figure to that of Fig. 2c for $d = 16 \mu\text{m}$ micropillars.



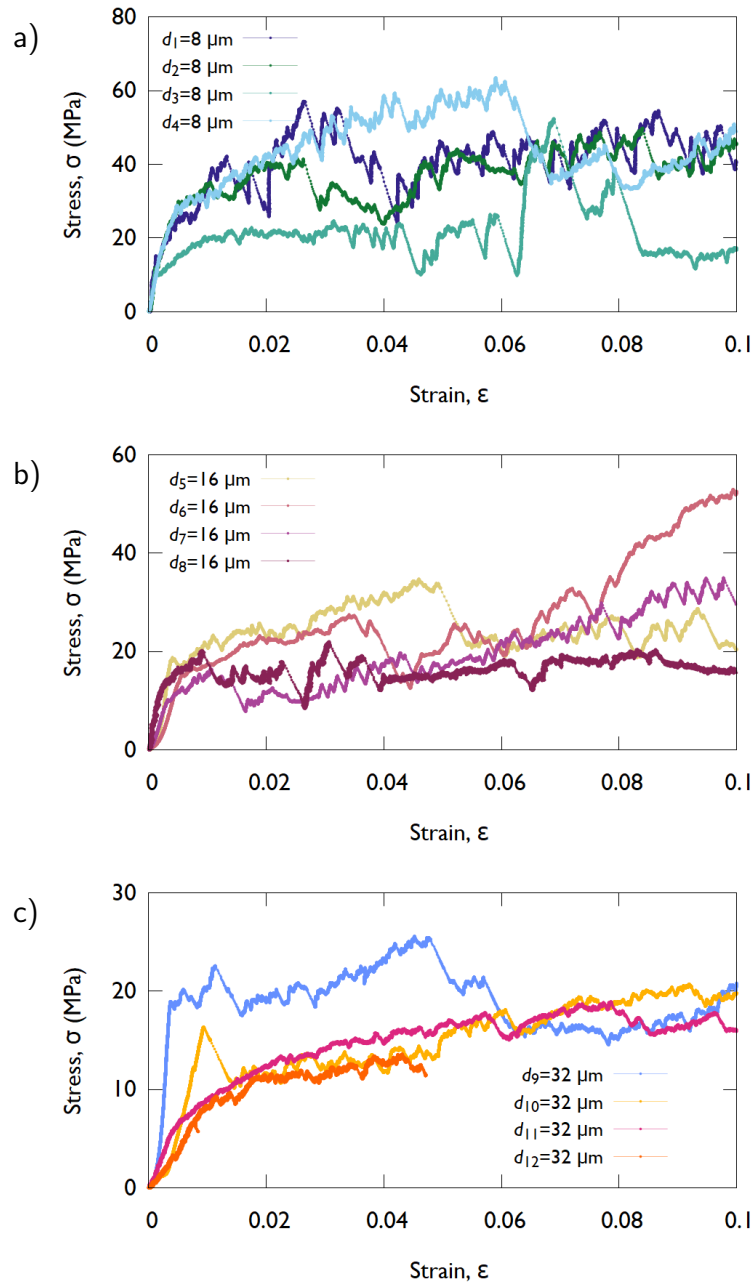
Extended Data Figure 4: **Aftershock and foreshock rates for $d = 8 \mu\text{m}$ and $d = 16 \mu\text{m}$ micropillars.** **a**, Aftershock rates r_{as} after main shocks of various energies E_{ms} for $d = 8 \mu\text{m}$ micropillars. **b**, Aftershock rates r_{as} of panel a) scaled with $E_{ms}^{0.5}$ for $d = 8 \mu\text{m}$ micropillars. **c**, Aftershock rates r_{as} after main shocks of various energies E_{ms} for $d = 16 \mu\text{m}$ micropillars. **d**, Aftershock rates r_{as} of panel a) scaled with $E_{ms}^{0.5}$ for $d = 16 \mu\text{m}$ micropillars. **e**, Foreshock rates r_{fs} before main shocks of various energies E_{ms} for $d = 8 \mu\text{m}$ micropillars. **f**, Foreshock rates r_{fs} before main shocks of various energies E_{ms} for $d = 16 \mu\text{m}$ micropillars.



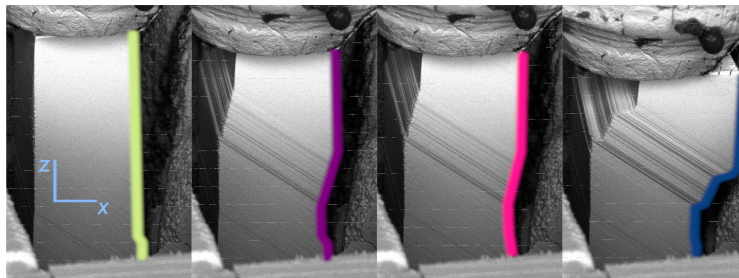
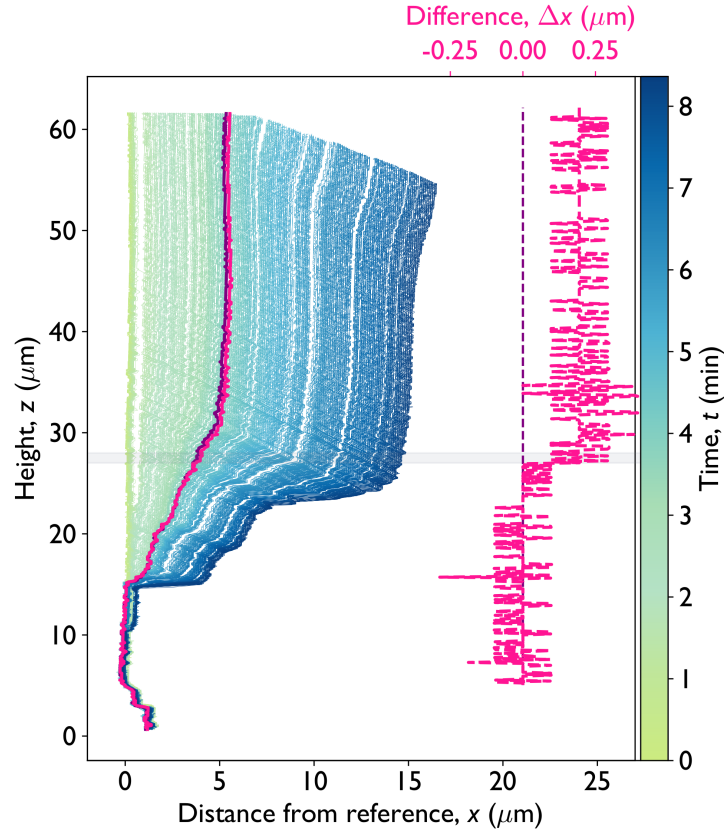
Extended Data Figure 5: **a**, A typical Kikuchi pattern collected from the sample used for the HR-EBSD evaluation. 20 regions of interest are marked with yellow squares. **b**, The resulting GND density map. Black point (in the middle) marks the reference pixel.



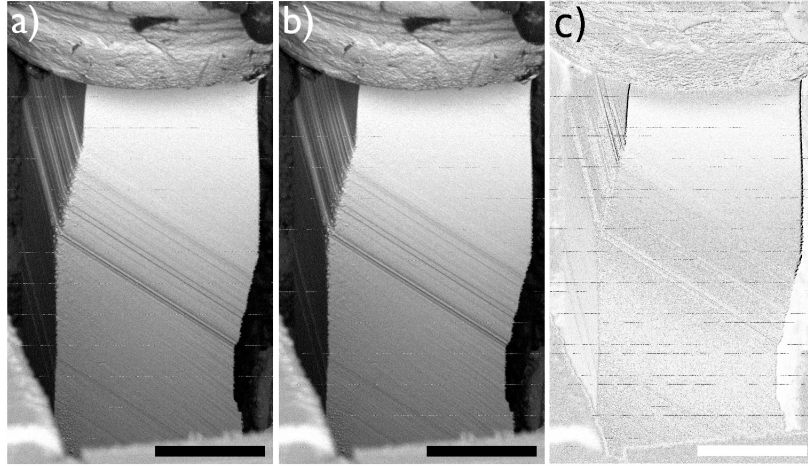
Extended Data Figure 6: **X-ray diffraction measurements on the original bulk Zn sample.** **a**, The measured X-ray line profile of the $(10\bar{1}1)$ reflection of the Zn single crystal. **b**, Second restricted moment M_2 as a function of $\ln q/q_0$, with $q_0 = 1 \text{ nm}^{-1}$. Dislocation density can be obtained from the linear fit from Eq. (1).



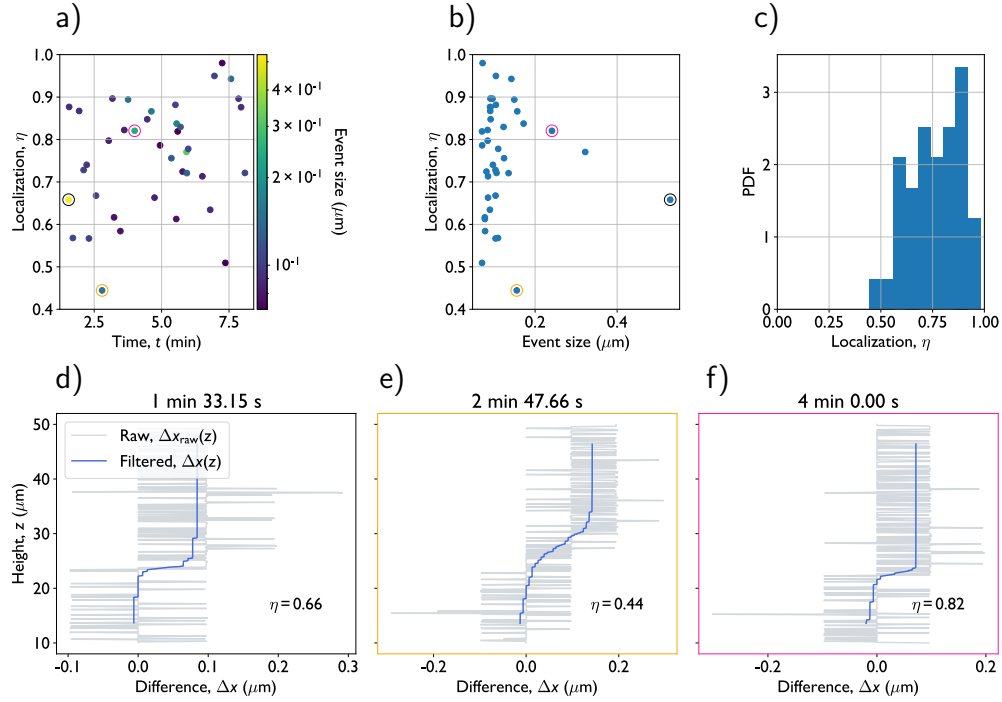
Extended Data Figure 7: **Exemplary stress-strain curves of micropillars of various sizes.** **a**, $d = 8 \mu\text{m}$, **b**, $d = 16 \mu\text{m}$ and **c**, $d = 32 \mu\text{m}$ pillars.



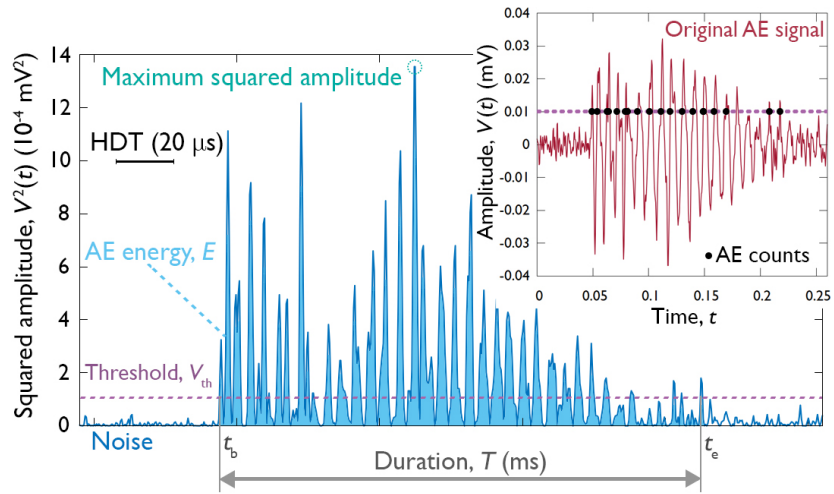
Extended Data Figure 8: **Time development of the right edge of the micropillar.** Distance from the reference line with the corresponding height as a function of time indicated by the colour for the micropillar shown in Fig. 1b. The purple and pink lines indicate the pillar shape before and after the stress drop investigated in Figs. 1c-e, respectively. The light gray horizontal line highlights the place where slip occurred.



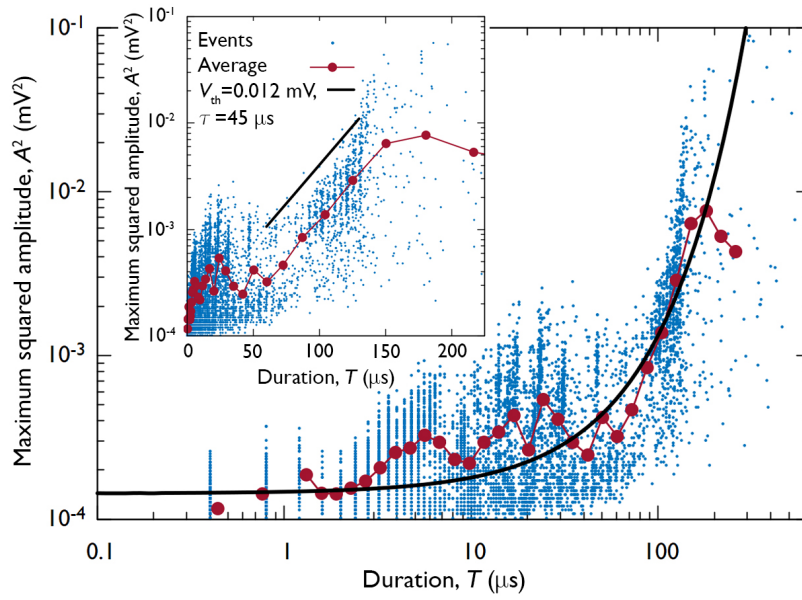
Extended Data Figure 9: **Locating spatial distribution of a strain burst.** **a, b,** Backscattered electron images of the micropillar before and after the stress drop analysed in Figs. 1c-e. The scale bar represents 20 μm . **c,** The difference of panels a) and b). The dark edges at the upper part of the pillar are due to plastic slip that occurred on the slip band highlighted in red in Fig. 1b.



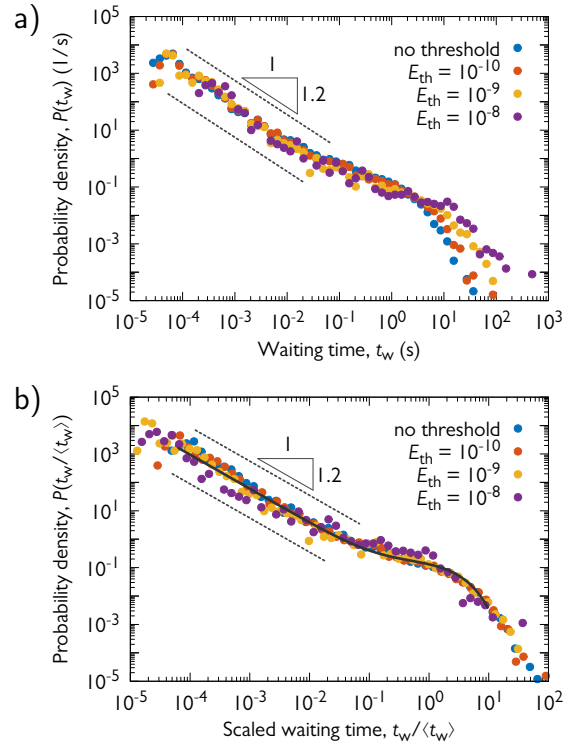
Extended Data Figure 10: **Analysis of strain localization on differential edge profiles.** **a**, Localization parameter η as a function of time t and event size $\Delta x(L) - \Delta x(0)$. The color scale refers to the event size $\Delta x(L) - \Delta x(0)$. **b**, Localization parameter η as a function of event size $\Delta x(L) - \Delta x(0)$. **c**, The probability distribution of the localization parameter η . **d-f**, Three exemplary $\Delta x_{\text{raw}}(z)$ (light gray) and the corresponding $\Delta x(z)$ (blue) profiles obtained using the method described in the text. The datapoints corresponding to the curves are circled with the same colour as the frame of the figures.



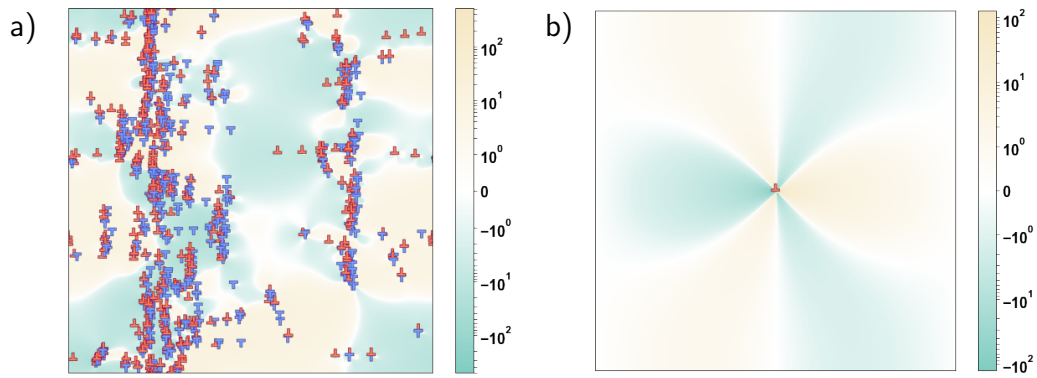
Extended Data Figure 11: **Parameters of a typical AE event.** Squared amplitude $V^2(t)$ of the AE signal as a function of time, showing the definitions of the AE parameters. The energy is the area of the region shaded in light blue. The inset presents the original waveform.



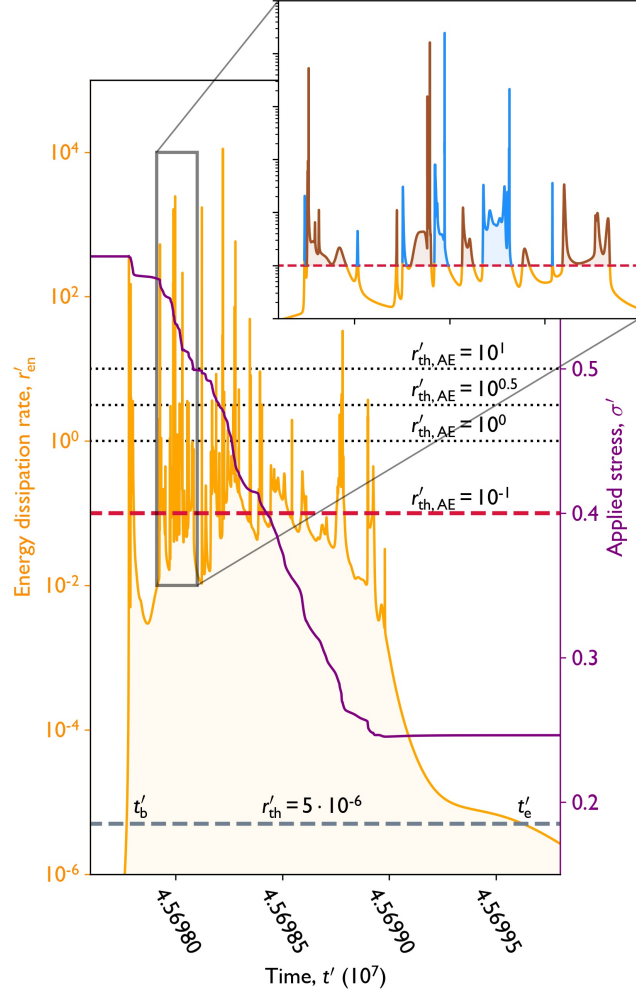
Extended Data Figure 12: **Analysis of AE signal attenuation.** Scatter plot of the maximum squared amplitude of individual AE events and their duration. The red data points represent the average relationship obtained by logarithmic binning with respect to the signal duration. Black solid line corresponds to the fit according to Eq. (8).



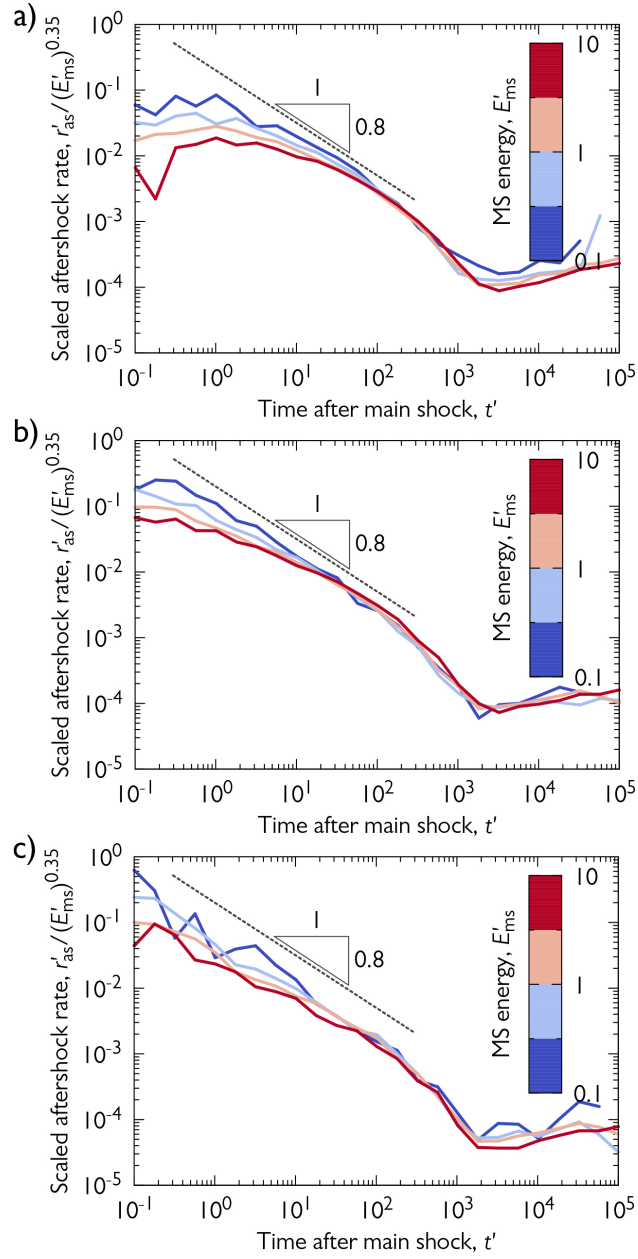
Extended Data Figure 13: **Effect of thresholding on waiting time distributions of $d = 32 \mu\text{m}$ micropillars.** **a**, Waiting time distributions for AE events with energies larger than E_{th} . **b**, Distributions of panel a) re-scaled with the average waiting time of the events. The master curve fitting the collapsed curves is identical to that of Fig. 3f.



Extended Data Figure 14: **2D discrete dislocation dynamics simulations.** **a**, An exemplary configuration with 512 positive (red) and 512 negative (blue) sign dislocations. The background colour and the colour scale refers to the internal shear stress generated by the individual dislocations. **b**, Shear stress field of an individual positive sign dislocation σ'_{ind} with periodic boundary conditions applied at all edges of the square-shaped simulation area.



Extended Data Figure 15: **Event individualization in DDD simulations.** The time dependence of the energy dissipation rate r'_{en} during an exemplary plastic event (also shown in Supplementary Video 3). The thick horizontal black line denotes the threshold r'_{th} used for identification of a plastic event, whereas dotted horizontal black lines refer to thresholds $r'_{\text{th,AE}}$ used to individualize emulated AE bursts. The inset shows the identified AE bursts that took place during the stress drop at $r'_{\text{th,AE}} = 0.1$ (shown with dotted red line in the main panel). The areas shaded alternately in blue and red correspond to the energies of the emulated AE events.



Extended Data Figure 16: **Effect of thresholding on the emulated scaled aftershock rates in DDD simulations.** Aftershock rates r'_{as} after main shocks with different energies E'_{ms} scaled with $(E'_{ms})^{0.35}$. The panels correspond to rates observed at different thresholds $r'_{th,AE}$ used for the emulation of AE events: **a**, $r'_{th,AE} = 0.1$. **b**, $r'_{th,AE} = 1$. **c**, $r'_{th,AE} = 10$.

Quantity	length	stress	strain	time
Unit	$\rho^{-0.5}$	$Gb\rho^{0.5}$	$b\rho^{0.5}$	$(Gb^2M\rho)^{-1}$

Extended Data Table 1: **Units of the dimensionless quantities used in the simulations.**

Property	Earthquakes	Dislocation avalanches
Mechanism	Slip / crack	Dislocation movement
Expanse	in plane	in plane
Typical amplitude	m	nm
Typical reach	km	μm
Typical duration	minute – month	ms – s
Typical frequency	Hz	MHz
Size distribution	Gutenberg-Richter	Gutenberg-Richter
Aftershocks	Omori- and productivity law	Omori- and productivity law

Extended Data Table 2: **Comparison between earthquake and dislocation avalanche properties.**

764 **Supplementary information**

765 Video 1: In situ SEM video of a compression of a $d = 8 \mu\text{m}$ micropillar
766 together with the measured force and the rate of AE events and released
767 AE energies. The ultrasonic AE signal recorded during the compression was
768 transformed into audible frequency domain that appears as a crackling noise.

769 Video 2: Representative DDD simulation of $N = 1024$ dislocations subjected
770 to increasing shear stress with the protocol described in Methods. Dislocation
771 configuration is seen in top right panel. Red and blue colours refer to the sign
772 of the dislocations and the background colour with the colour scale represents
773 the internal shear stress generated by the dislocations. The force-time curve
774 is shown in the left panel together with the emulated AE count rate (see
775 Methods for details).

776 Video 3: Slowed down video of a representative plastic event (stress drop)
777 from Supplementary Video 2.

778 Video 4: Edge detection during the deformation of a $32 \mu\text{m}$ micropillar. Left
779 panel shows the original video recorded by the SEM. In the left panel the
780 green line is the reference (see Methods for details) and the blue line is the
781 detected edge of the micropillar.

782 **References**

- 783 ¹Uchic, M. D., Dimiduk, D. M., Florando, J. N. & Nix, W. D. Sample
784 Dimensions Influence Strength and Crystal Plasticity. *Science* **305**, 986–
785 989 (2004).
- 786 ²Volkert, C. A. & Lilleodden, E. T. Size effects in the deformation of sub-
787 micron Au columns. *Philos. Mag.* **86**, 5567–5579 (2006).
- 788 ³Miguel, M.-C., Vespignani, A., Zapperi, S., Weiss, J. & Grasso, J.-R. Inter-
789 mittent dislocation flow in viscoplastic deformation. *Nature* **410**, 667–671
790 (2001).
- 791 ⁴Weiss, J. & Marsan, D. Three-dimensional mapping of dislocation
792 avalanches: clustering and space/time coupling. *Science* **299**, 89–92
793 (2003).
- 794 ⁵Dimiduk, D. M., Woodward, C., LeSar, R. & Uchic, M. D. Scale-free
795 intermittent flow in crystal plasticity. *Science* **312**, 1188–1190 (2006).
- 796 ⁶Csikor, F. F., Motz, C., Weygand, D., Zaiser, M. & Zapperi, S. Disloca-
797 tion avalanches, strain bursts, and the problem of plastic forming at the
798 micrometer scale. *Science* **318**, 251–254 (2007).
- 799 ⁷Orowan, E. Zur kristallplastizität. iii. *Z. Phys.* **89**, 634–659 (1934).
- 800 ⁸Polanyi, M. Über eine Art Gitterstörung, die einen Kristall plastisch
801 machen könnte. *Z. Phys.* **89**, 660–664 (1934).
- 802 ⁹Taylor, G. I. The mechanism of plastic deformation of crystals. Part
803 I.—Theoretical. *P. R. Soc. London* **145**, 362–387 (1934).

- 804 ¹⁰ Scruby, C. B. An introduction to acoustic emission. *J. Phys. E* **20**, 946
805 (1987).
- 806 ¹¹ Weiss, J. *et al.* Evidence for universal intermittent crystal plasticity from
807 acoustic emission and high-resolution extensometry experiments. *Phys.*
808 *Rev. B* **76**, 224110 (2007).
- 809 ¹² Gutenberg, B. & Richter, C. F. Magnitude and energy of earthquakes.
810 *Ann. Geofis.* **9** (1956).
- 811 ¹³ Utsu, T. Representation and Analysis of the Earthquake Size Distribution:
812 A Historical Review and Some New Approaches. *Pure Appl. Geophys.* **155**,
813 509–535 (1999).
- 814 ¹⁴ Utsu, T., Ogata, Y. & Matsu'ura, R. S. The Centenary of the Omori
815 Formula for a Decay Law of Aftershock Activity. *J. Phys. Earth* **43**, 1–33
816 (1995).
- 817 ¹⁵ Guglielmi, A. V. Interpretation of the Omori law. *Izv., Phys. Solid Earth*
818 **52**, 785–786 (2016).
- 819 ¹⁶ Helmstetter, A. Is earthquake triggering driven by small earthquakes?
820 *Phys. Rev. Lett.* **91**, 058501 (2003).
- 821 ¹⁷ Baró, J. *et al.* Statistical Similarity between the Compression of a Porous
822 Material and Earthquakes. *Phys. Rev. Lett.* **110**, 088702 (2013).
- 823 ¹⁸ Meng, F., Wong, L. N. Y. & Zhou, H. Power law relations in earthquakes
824 from microscopic to macroscopic scales. *Sci. Rep.* **9**, 10705 (2019).

- 825 ¹⁹ Jones, L. M. & Molnar, P. Some characteristics of foreshocks and their pos-
826 sible relationship to earthquake prediction and premonitory slip on faults.
827 *J. Geophys. Res.-Sol. Ea.* **84**, 3596–3608 (1979).
- 828 ²⁰ Weiss, J. & Miguel, M.-C. Dislocation avalanche correlations. *Materials*
829 *Science and Engineering: A* **387**, 292–296 (2004).
- 830 ²¹ Bak, P., Christensen, K., Danon, L. & Scanlon, T. Unified scaling law for
831 earthquakes. *Phys. Rev. Lett.* **88**, 178501 (2002).
- 832 ²² Karsai, M., Kaski, K., Barabási, A.-L. & Kertész, J. Universal features of
833 correlated bursty behaviour. *Sci. Rep.* **2**, 1–7 (2012).
- 834 ²³ Corral, A. Long-term clustering, scaling, and universality in the temporal
835 occurrence of earthquakes. *Phys. Rev. Lett.* **92**, 108501 (2004).
- 836 ²⁴ Houdoux, D., Amon, A., Marsan, D., Weiss, J. & Crassous, J. Micro-slips
837 in an experimental granular shear band replicate the spatiotemporal char-
838 acteristics of natural earthquakes. *Communications Earth & Environment*
839 **2**, 1–11 (2021).
- 840 ²⁵ Ispánovity, P. D. *et al.* Avalanches in 2D dislocation systems: Plastic
841 yielding is not depinning. *Phys. Rev. Lett.* **112**, 235501 (2014).
- 842 ²⁶ Csikor, F. F., Zaiser, M., Ispánovity, P. D. & Groma, I. The role of density
843 fluctuations in the relaxation of random dislocation systems. *J. Stat. Mech.*
844 **2009**, P03036 (2009).
- 845 ²⁷ Zaiser, M. & Sandfeld, S. Scaling properties of dislocation simulations in
846 the similitude regime. *Model. Simul. Mater. Sci.* **22**, 065012 (2014).

- 847 ²⁸ Lehtinen, A., Costantini, G., Alava, M. J., Zapperi, S. & Laurson, L.
848 Glassy features of crystal plasticity. *Phys. Rev. B* **94**, 064101 (2016).
- 849 ²⁹ Sethna, J. P., Dahmen, K. A. & Myers, C. R. Crackling noise. *Nature*
850 **410**, 242–250 (2001).
- 851 ³⁰ Weiss, J. *et al.* From mild to wild fluctuations in crystal plasticity. *Phys.*
852 *Rev. Lett.* **114**, 105504 (2015).
- 853 ³¹ Zhang, P. *et al.* Taming intermittent plasticity at small length scales. *Acta*
854 *Materialia* **128**, 351–364 (2017).
- 855 ³² Alcalá, J. *et al.* Statistics of dislocation avalanches in FCC and BCC met-
856 als: dislocation mechanisms and mean swept distances across microsample
857 sizes and temperatures. *Sci. Rep.* **10**, 1–14 (2020).
- 858 ³³ Uchic, M., Shade, P. & Dimiduk, D. Plasticity of micromoter-scale single
859 crystals in compression. *Annu. Rev. Mater. Res.* **39**, 361–386 (2009).
- 860 ³⁴ Britton, T. B. & Wilkinson, A. J. High resolution electron backscatter
861 diffraction measurements of elastic strain variations in the presence of
862 larger lattice rotations. *Ultramicroscopy* **114**, 82–95 (2012).
- 863 ³⁵ Groma, I. & Székely, F. Analysis of the asymptotic properties of X-ray line
864 broadening caused by dislocations. *J. Appl. Cryst.* **33**, 1329–1334 (2000).
- 865 ³⁶ Borbély, A. & Groma, I. Variance method for the evaluation of particle
866 size and dislocation density from X-ray Bragg peaks. *Appl. Phys. Lett.* **79**,
867 1772–1174 (2001).

- 868 ³⁷ Groma, I. & Borbély, A. X-ray peak broadening due to inhomogeneous
869 dislocation distributions. In *Diffraction Analysis of the Microstructure of*
870 *Materials*, 287–307 (Springer, 2004).
- 871 ³⁸ Dragomir, I. C. & Ungár, T. Contrast factors of dislocations in the hexago-
872 nal crystal system. *Journal of Applied Crystallography* **35**, 556–564 (2002).
- 873 ³⁹ Borbély, A., Dragomir-Cernatescu, J., Ribárik, G. & Ungár, T. Computer
874 program ANIZC for the calculation of diffraction contrast factors of dis-
875 locations in elastically anisotropic cubic, hexagonal and trigonal crystals.
876 *Journal of Applied Crystallography* **36**, 160–162 (2003).
- 877 ⁴⁰ Hegyi, A. I. *et al.* Micron-Scale Deformation: A Coupled In Situ Study of
878 Strain Bursts and Acoustic Emission. *Microsc. Microanal.* **23**, 1076–1081
879 (2017).
- 880 ⁴¹ Kalácska, S. *et al.* Investigation of geometrically necessary dislocation
881 structures in compressed Cu micropillars by 3-dimensional HR-EBSD. *Mat.*
882 *Sci. Eng. A.* **770**, 138499 (2020).
- 883 ⁴² Bradski, G. The OpenCV Library. *Dr. Dobb's J.* **25**, 120–125 (2000).
- 884 ⁴³ Tüzes, D., Ispánovity, P. D. & Zaiser, M. Disorder is good for you: the
885 influence of local disorder on strain localization and ductility of strain
886 softening materials. *International Journal of Fracture* **205**, 139–150 (2017).
887 URL <https://doi.org/10.1007/s10704-017-0187-1>.
- 888 ⁴⁴ Heiple, C. R. & Carpenter, S. H. Acoustic emission produced by defor-
889 mation of metals and alloys - A review. *J. Acoustic Emission* **6**, 177–237
890 (1987).

- 891 ⁴⁵ Jordi, B. *et al.* Experimental Evidence of Accelerated Seismic Release
892 without Critical Failure in Acoustic Emissions of Compressed Nanoporous
893 Materials. *Phys. Rev. Lett.* **120**, 245501 (2018).
- 894 ⁴⁶ Vu, C. C., & Weiss, J. Assymmetric Damage Avalanche Shape in Quasibrittle
895 Materials and Subavalanche (Aftershock) Clusters. *Phys. Rev. Lett.* **125**,
896 105502 (2020).
- 897 ⁴⁷ Kanamori, H. & Brodsky, E. E. The physics of earthquakes. *Reports on*
898 *Progress in Physics* **68**, 1429 (2004).
- 899 ⁴⁸ Hirth, J. P. & Lothe, J. *Theory of Dislocations* (John Willey & Sons, New
900 York, 1982), 2nd edn.
- 901 ⁴⁹ Bakó, B., Groma, I., Györgyi, G. & Zimányi, G. Dislocation patterning:
902 The role of climb in meso-scale simulations. *Comp. Mater. Sci.* **38**, 22–28
903 (2006).
- 904 ⁵⁰ Péterffy, G. & Ispánovity, P. D. An efficient implicit time integration
905 method for discrete dislocation dynamics. *Model. Simul. Mater. Sci.* **28**,
906 035013 (2020).
- 907 ⁵¹ Shan, Z., Mishra, R. K., Asif, S. S., Warren, O. L. & Minor, A. M. Mechan-
908 ical annealing and source-limited deformation in submicrometre-diameter
909 ni crystals. *Nature materials* **7**, 115–119 (2008).
- 910 ⁵² Tang, H., Schwarz, K. & Espinosa, H. Dislocation-source shutdown and
911 the plastic behavior of single-crystal micropillars. *Physical review letters*
912 **100**, 185503 (2008).

⁹¹³ ⁵³ Harris, C. R. *et al.* Array programming with NumPy. *Nature* **585**, 357–362
⁹¹⁴ (2020).